Titre: Title:	Specialty Optical Fibers from Visible to Terahertz
Auteur: Author:	Roya Gachiloo
Date:	2025
Type:	Mémoire ou thèse / Dissertation or Thesis
Référence: Citation:	Gachiloo, R. (2025). Specialty Optical Fibers from Visible to Terahertz [Mémoire de maîtrise, Polytechnique Montréal]. PolyPublie. https://publications.polymtl.ca/71477/

URL de PolyPublie: PolyPublie URL:	https://publications.polymtl.ca/71477/
Directeurs de recherche: Advisors:	Maksim A. Skorobogatiy
Programme: Program:	Génie physique

POLYTECHNIQUE MONTRÉAL
affiliée à l'Université de Montréal

Specialty Optical Fibers from Visible to Terahertz

ROYA GACHILOO
Département de génie physique

Mémoire présenté en vue de l'obtention du diplôme de *Maîtrise ès sciences appliquées*
Génie physique

Décembre 2025

POLYTECHNIQUE MONTRÉAL
affiliée à l'Université de Montréal

Ce mémoire intitulé :

Specialty Optical Fibers from Visible to Terahertz

présenté par **Roya GACHILOO**
en vue de l'obtention du diplôme de *Maîtrise ès sciences appliquées*
a été dûment accepté par le jury d'examen constitué de :

Sébastien FRANCOEUR, président
Maksim SKOROBOGATIY, membre et directeur de recherche
Lucien WEISS, membre

ACKNOWLEDGEMENTS

First, I would like to express my deepest gratitude to Prof. Maksim Skorobogatiy for giving me the opportunity to be part of his research group. Thank you for sharing your valuable knowledge and for your patience.

I am also very grateful to all my colleagues especially Vladislav Ulitko and Babak Yahyapour for their support. I would additionally like to express my sincere thanks to Guofu Xu, whose guidance was truly invaluable.

My sincere thanks also go to my defense committee, Prof. Sébastien Francoeur and Prof. Lucien Weiss, for kindly agreeing to evaluate this thesis and providing their valuable feedback.

Finally, my deepest thanks go to my family and my friends. Your constant support has carried me through this journey.

RÉSUMÉ

Cette thèse explore la fabrication et la caractérisation de fibres optiques spéciales à travers deux axes principaux. La première partie porte sur le développement d'une méthode simple et peu coûteuse pour produire des fibres polymères à émission latérale, capables de diffuser la lumière de manière contrôlée le long de leur surface, sans utiliser des techniques de fabrication complexes. La Deuxième partie propose une approche pour la caractérisation de guides d'onde térahertz, afin de développer une méthode robuste d'évaluation de leurs performances de transmission.

La première partie de ce travail est consacrée à la fabrication de fibres optiques polymères à émission latérale par abrasion de surface à l'aide de papier de verre. Les études expérimentales ont montré que cette méthode permet d'améliorer efficacement l'émission latérale ; toutefois, cette méthode ne garantit toutefois ni une émission uniforme ni un contrôle complet de celle-ci. Des recherches supplémentaires sont donc nécessaires pour améliorer l'uniformité de l'émission latérale et permettre le contrôle de paramètres tels que le profil de diffusion et la distribution de l'émission.

La seconde partie est consacrée à la caractérisation de guides d'onde métalliques à cœur creux dans le domaine térahertz. Les mesures ont été réalisées à l'aide d'un système de spectroscopie térahertz en onde continue et la méthode du cutback a permis de déterminer l'atténuation en fonction de la fréquence à partir de guides de différentes longueurs. Les résultats confirment l'efficacité de cette méthode pour caractériser ce type de structures. Toutefois, dans le cas des guides multimodaux étudiés ici, l'absence d'un dispositif de couplage optimisé limite la reproductibilité des mesures. L'intégration d'un système de couplage plus performant s'avère essentielle pour obtenir une caractérisation fiable.

Dans l'ensemble, ces travaux contribuent à l'avancement des technologies de fibres optiques spéciales, en couvrant à la fois le domaine visible et le domaine térahertz. Les fibres polymères à émission latérale ouvrent des perspectives pour les applications nécessitant une diffusion contrôlée de la lumière, tandis que l'étude des guides térahertz apporte des informations essentielles sur leurs pertes de propagation, un paramètre clé pour le développement de futures liaisons de communication.

ABSTRACT

This thesis focuses on the fabrication and characterization of specialty optical fibers through two studies. The first aims to develop a simple and inexpensive approach for producing side-emitting fibers with uniform light emission. The second introduces a method for characterizing waveguides with the goal of providing a reliable technique for evaluating waveguide attenuation.

The first part of this work focuses on the fabrication of side-emitting polymer optical fibers using a simple surface modification approach. By modification of the fiber surface with abrasive papers, lateral emission of light is achieved without the need for complex or costly fabrication processes. Experimental studies demonstrated that this method can enhance side emission efficiently; however, it does not yet provide uniform or fully controllable emission. Further investigation is therefore required to improve the uniformity of side emission and to enable control over parameters such as the scattering profile and emission distribution.

The second part of the thesis aims to characterize a hollow-core metallic waveguide. The continuous-wave terahertz spectroscopy system was employed to measure transmission through waveguides of different lengths, enabling the use of the cutback method to extract frequency-dependent attenuation. The results demonstrate that this approach can be applied effectively for the characterization of terahertz waveguides. However, for the waveguides studied here, further improvements to the experimental setup are required, since their multimode nature prevents consistent and reproducible measurements. In particular, the development and integration of an efficient coupling device will be necessary to achieve reliable characterization of these structures.

Together, these studies contribute to the understanding and advancement of specialty fiber technologies across distinct frequency ranges. The side-emitting polymer optical fibers are suitable for applications requiring lateral light emission in the visible range, while the waveguide measurements provide insights into attenuation characterization that are critical for the development of efficient terahertz communication links.

TABLE OF CONTENTS

LIST OF TABLES

LIST OF FIGURES

LIST OF SYMBOLS AND ACRONYMS

TE	Transverse Electric
TM	Transverse Magnetic
ID	Inner Diameter
3D	Three-Dimensional
THz	Terahertz
CW	Continuous Wave
TDS	Time-Domain spectroscopy
POF	Polymer Optical Fibers
SEPOF	Side-Emitting Polymer Optical Fiber
TIR	Total Internal Reflection
mTIR	Modified Total Internal Reflection
PBG	Photonic Band Gap
DFB	Distributed-feedback laser
TiO2	Titanium Dioxide
PMMA	Polymethyl Methacrylate
FWHM	Full Width at Half Maximum
PTFE	Polytetrafluoroethylene
PVDF	Polyvinylidene Fluoride

LIST OF APPENDICES

CHAPTER 1 INTRODUCTION

1.1 Motivation

Optical fiber technology has been one of the key innovations in modern engineering, used as the backbone of today's global communication infrastructure. By guiding light through flexible dielectric waveguides with minimal loss, optical fibers enable the transmission of vast amounts of information over long distances with high bandwidth, speed, and signal stability. Beyond telecommunications, optical fibers have become indispensable in sensing, imaging, and industrial monitoring due to their compactness, immunity to electromagnetic interference, and ability to function in harsh environments. Contemporary research now extends beyond increasing data rates and transmission distances, and also addresses emerging priorities such as flexibility, scalability, cost efficiency, and communication security, ensuring that optical fiber technology continues to adapt to the growing demands of a globally connected world.

The focus of this thesis is on the development and characterization of specialty optical fibers operating in the visible and terahertz (THz) frequency ranges. The work is divided into two main parts. The first part is dedicated to the fabrication and characterization of side-emitting polymer optical fibers, while the second part focuses on the development of a reliable method for evaluating the attenuation of waveguides in the THz frequency range.

This project was initiated with the design and fabrication of side-emitting polymer optical fibers in collaboration with the research group of Prof. David Plant at McGill University. The goal was to fabricate a polymer optical fiber that emits light uniformly along its surface, ultimately enabling its use in slip-ring communication systems for data transfer across rotating interfaces.

The work began with the simplest possible geometry, a solid PMMA rod-in-air fiber, fabricated using the fiber drawing technique. After obtaining the base fiber, the next step was to introduce the scatterers and enable side emission. Among various modification methods, a surface-abrasion technique using abrasive paper was selected for its simplicity and low cost. The aim of the initial experiments was to understand the relationship between the surface treatment parameters and the resulting emission profile, and to identify the limits of this method in achieving uniform side emission.

A theoretical analysis was first conducted to determine the scattering profile required for uniform side emission along the fiber. If a fiber is modified identically along its length, the

side-emitted light will naturally be strongest near the input and decay exponentially with distance as the guided light is progressively lost. It showed that the scattering coefficient must vary gradually with distance from the light source to compensate for power decay along the fiber. Based on this model, the fiber was divided into sections, and the number of surface scratches in each section was calculated to follow the theoretical distribution of scatterers. For the experimental evaluation, PMMA fibers with diameters between 0.8-1.5 mm were fabricated and then modified using abrasive papers of different grit sizes. The fibers were divided into segments, each scratched with a specific number of passes to adjust the local scattering density. A supercontinuum light source was used to illuminate the fiber, and the side-emitted light intensity was measured along its length using an optical power meter. To ensure reliable comparison, the fiber was rotated in four orientations, and the average emission intensity was recorded. The results confirmed that surface modification substantially increased side emission, although achieving a fully uniform emission profile remained challenging. Several systematic experiments were performed to identify the optimal parameters for surface modification. Rough abrasive papers (grit 240 and 320) generated strong emissions after a few passes but quickly degraded the fiber surface, blocking light propagation. Smoother papers (grit 400 and 600) produced weaker but more stable emission and enabled finer control. A combination of different grit sizes provided the best outcome. Initial scratches with smoother paper, followed by localized rougher passes, enhanced emission without destroying guiding properties. However, despite significant improvement, the emission along the fiber remained non-uniform, with higher scattering near the input end.

To better understand the cause of non-uniformity, a cutback technique was used to measure the intrinsic optical losses of the PMMA material. Furthermore, additional experiments showed that precise control of the surface scattering profile is critical for obtaining a balanced emission. Efforts were also made to improve the measurement reliability. A 3D-printed integrating reflective surface was designed to collect light uniformly from all sides of the fiber, eliminating the need for rotation during measurements. Preliminary tests showed improved signal collection efficiency, although further calibration was required before integrating the device into the main experiments. Through these investigations, a practical understanding was developed of how surface modification parameters, scattering mechanisms, and material properties determine side emission in polymer fibers. The findings demonstrated that surface abrasion is a feasible and low-cost method to induce side emission, but fine control and reproducibility remain limited.

The results of this research were presented at the 35th COPL Annual Conference, where the work received the first prize in the category of Optical Fibers and Devices. Following this achievement, the next planned phase of the project aimed to extend the study by fabricating

different types of polymer fibers with more advanced material compositions and modification techniques. In particular, a polycarbonate (PC) core with a PMMA cladding fiber was fabricated using the fiber drawing technique. The subsequent modification step was planned to employ a TiO_2-based surface treatment, a more complex approach intended to introduce controlled scattering centers through nanoparticle deposition rather than mechanical abrasion. However, the collaboration with the McGill research group was discontinued before this stage could be completed, and the project did not progress to the implementation of this modification method.

The second part of this thesis extended the focus from the visible range to the THz regime, where the goal was to establish a reliable and repeatable measurement method for the characterization of THz waveguides, particularly to evaluate attenuation losses. This study was carried out as part of a collaboration with Attotude, a company specializing in THz technology and instrumentation. The project began with the characterization of copper hollow core waveguides using a continuous-wave (CW) THz spectroscopy system. To ensure appropriate coupling and minimize measurement uncertainty, the first step was to determine the beam diameter of the THz radiation generated by the system. This was achieved experimentally using the knife-edge technique, where a metallic blade mounted on a micrometre translation stage was moved across the THz beam while recording the transmitted signal at frequencies between 100 GHz and 1 THz. The collected data were used to determine the beam diameter. This step was crucial for selecting suitable focusing optics, leading to the choice of the appropriate PTFE lens, which provided sufficient aperture to capture and focus the entire beam throughout the studied frequency range.

Once the beam parameters were established, the transmission measurements of copper waveguides were performed using the CW THz system. Three copper tubes with inner diameters of 3 mm and lengths of 31 cm, 117 cm, and 204 cm were investigated using the cutback technique to extract the attenuation. The setup incorporated parabolic mirrors and PTFE lenses to focus the THz beam at the entrance and exit of each waveguide, while aluminum plates around the apertures minimized stray radiation. Each waveguide was tested sequentially under identical conditions to minimize environmental influences such as temperature drift or electronic instability. The transmitted power spectra clearly showed decreasing signal levels with increasing waveguide length, and the attenuation increased with frequency. These results confirmed that the implemented method successfully extracted the attenuation characteristics of THz hollow-core waveguides within the frequency range of interest.

However, as the experiments progressed, signal reproducibility issues were encountered. Despite maintaining identical alignment and coupling parameters, successive measurements

yielded noticeable variations in transmission spectra. To identify the cause, several diagnostic tests were performed. The system calibration was verified, integration time and step size parameters were varied, and the experimental configuration was modified by introducing four flat mirrors to redirect the beam for monitoring stability without altering the setup. The stability tests confirmed that the THz system itself was stable. Further theoretical analysis revealed that the copper waveguides used in this study were multimode structures. These findings demonstrated that, while the implemented cutback-based measurement procedure is effective for determining the waveguide losses, the current configuration is not fully suitable for multimode waveguides, where mode coupling introduces significant uncertainty. Although the multimode nature of the waveguides limited measurement reproducibility, the study provided valuable insights into the experimental challenges of THz waveguide testing and outlined the improvements required for future investigations, particularly the need for controlled mode excitation and optimized coupling schemes for single-mode operation in the THz range.

1.2 Side-Emitting Polymer Fibers

Side-emitting polymer optical fibers (POFs) are a special kind of optical fibers designed to emit light along their length. Similar to conventional optical fibers that confine light by total internal reflection along their entire length, side-emitting fibers also guide light but allow a portion of the radiation to escape through their cylindrical outer surface [2].

Early studies on side-emitting optical fibers date back to the 1990s, beginning with the work on silica fibers. Hasselgren *et al.* [3] investigated the potential of using these fibers in photodynamic therapy. They modified a conventional SiO_2 fiber by removing the cladding of 30mm of the end of the fiber and replacing it with a thin layer of optical epoxy mixed with TiO_2 powder. Since the refractive index of the epoxy was higher than that of the fiber core, the condition for total internal reflection was no longer satisfied, and light was coupled out of the fiber core into the new cladding and scattered out of the fiber cladding by TiO_2 particles. The research on side-emitting fibers continued with Spigulis *et al.* works [4] investigating the light diffusive fiber tips on silica fibers for local irradiation of tissues by lasers. In their subsequent works [5–7], side-emitting silica fibers were fabricated by doping the cladding with scattering additives and the potential applications for clinical use were investigated. The researchers also introduced a simplified exponential model for side emission,

discussed the exponential decrease in side emission intensity with the length of the fiber. To overcome this limitation, they suggested practical design approaches including dual-end coupling, use of a reflector at the end of the fiber and gradually increasing the scattering efficiency

with the fiber length. Side-emitting fiber research was not limited to silica. Side-emitting polymer optical fibers (SEPOF) have attracted growing attention due to their versatility, enabling applications beyond conventional end emission. To date, they are widely used in applications such as biomedical sensing, imaging and optical communication.

1.2.1 Light Emission Mechanisms and Fabrication Methods.

In side-emitting polymer optical fibers, lateral light emission is engineered by methods that deliberately hinder total internal reflection. Side emission in polymer optical fibers can be understood with reference to total internal reflection (TIR) at the core–cladding boundary of a fiber. Let n_{core} and n_{clad} denote the refractive indices of the core and cladding, respectively, and let θ be the internal angle of incidence (measured from the normal at the interface). TIR is sustained only when $\theta \geq \theta_{\text{crit}}$,

where

$$\theta_{\text{crit}} = \sin^{-1}\left(\frac{n_{\text{clad}}}{n_{\text{core}}}\right) \tag{1.1}$$

If the incidence angle decreases below θ_{crit}, the TIR condition is not satisfied and light leaks into the cladding. These nonguided modes then couple to radiation modes and are emitted laterally from the surface of the fiber, producing the side emission. Therefore, in side-emitting optical fibers (SEOFs), the design objective is to decrease the incidence angle below the critical angle to allow light leakage. The methods to change the incidence angle can be categorized in four main categories [8]: bulk scattering, surface perforation, bending, and luminescence.

Bulk Scattering One way to change the light path is to introduce the scattering centers into the fiber. The scattering properties can be inherent to the material (e.g., Mie scattering due to long molecular chains or Rayleigh scattering due to subwavelength molecular irregularities) or can be induced by adding substances or dopants such as microparticles or nanoparticles. The concentration of particles, shape and refractive index influence the emission strength [9,10]. Controlling the distribution of the particles over the fiber length enables uniform illumination. Scattering particles can be added to the fiber in the fabrication process of POF, like doping the fiber core or clad with scattering particles or as a post-processing step, like the treatment with a femtosecond laser. Side emission in POFs can be realized by adding the scattering particle to the core or cladding. The scattering particles can be made from organic and inorganic materials with light scattering properties or synthetic materials [8, 10, 11]. In cladding doping, unlike in core doping, the light ray is scattered upon

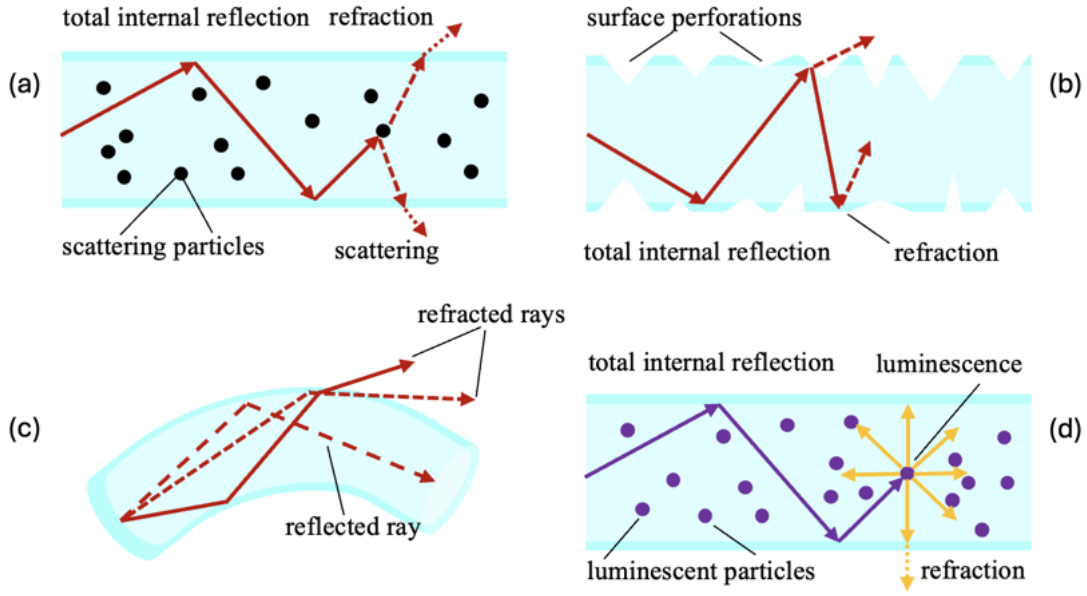

Figure 1.1 Reflection and refraction in side-emitting optical fibers: (a) refraction due to bulk scattering, (b) refraction due to surface perforations, (c) refraction due to bending and (d) refraction due to luminescence.

interaction at the core–cladding interface whenever it encounters a scattering particle. The intermediate layer between core and cladding can also contain the scattering particles. The size of the inserted microparticles varies between 50 and 2000 nm, so that both Rayleigh scattering and Mie scattering can occur. In a typical fabrication process, SEPOFs are fabricated by melting polymer granules, mixing them with scattering particles, and completing the process in a co-extrusion step. Depending on whether the core or cladding is doped, the scattering particles are compounded into the corresponding material, and the particle type, size, and concentration are selected based on the desired emission characteristics. Defects also act as the scattering centers in POFs [8]. These defects act as refractive index disturbances in the fiber core and scatter incident light, resulting in side emission from the fiber surface [11, 12]. Focusing a femtosecond or picosecond laser on the polymer (ex., by use of a microscopic objective) creates three-dimensional hollow structures below the fiber surface. The geometry and texture of the cavity and, therefore, the profile of surface activation in the fiber core depend on the laser power, the pulse energy, the number of pulses per interaction point and the distance between two interaction points [13–15].

Surface Perforation Surface treatment of the fiber with sandblasting, applying mechanical pressure, or other physical microstructuring techniques introduces controlled roughness at the core-cladding boundary, perturbing TIR and enhancing lateral emission. The resulting surface features can range from micro-perforations to notches or grooves, and their depth, number, and geometry determine the scattering strength and direction of the emitted light [16–19]. Microperforations penetrate only slightly into the cladding and affect the core minimally, resulting in weak scattering. Larger notches, on the contrary, emit a higher proportion of light, and asymmetrically distributed perforations can lead to stronger emission on the side opposite the notch [2]. The direction of the notches relative to the fiber axis and the geometry of the notches also influence the emission. Notches angled against the light propagation direction scatter more light on the notch side, while those angled with propagation scatter to the opposite side [8]. Flat notches result in higher total internal reflection, while deeper or broader notches increase scattering [18]. Surface perforation can be in the form of discrete notches or continuous perforations, such as spiral defects along the fiber axis [20].

Different strategies are used to homogenize the emission along the fiber length. One method is to reduce the spacing between discrete notches with increasing distance from the source, while another is to gradually increase the notch areas with increasing distance from the light source by making the notches deeper. Both strategies can also be combined, and small microperforations are applied to achieve a smoother distribution of emission [8]. The choice of core and cladding materials also plays a key role, since different materials have different absorption spectra for laser radiation, different solubilities for different solvents, and also different scratch resistances.

Mechanical surface perforation of fibers can be achieved through various abrasive methods. Simple sanding with sandpaper, applied either manually or by machine, treats both the core and cladding, while milling cutters or disc-shaped tools are suitable for producing larger or asymmetric notches [16]. The most common approach, however, is particle blasting (sandblasting), in which fibers are exposed to high-speed abrasive particles such as quartz, metal, or corundum accelerated by compressed air. The abrasive stream roughens the fiber surface, and adhering particles are removed afterward, for example, using an air knife. In single-fiber processing, blasting is typically applied continuously, and by adjusting nozzle pressure or fiber feed speed, the degree of side-emission activation can be gradually controlled. For woven structures where POFs are used as planar light sources, CNC-controlled blasting nozzles allow precise and gradual surface treatment [21].

Chemical surface treatment of POFs can be achieved using either etchants or solvents, with the degree of modification depending on chemical concentration, temperature, and exposure

time [16]. Exposing polymers to etchants results in material degradation through a chemical reaction between the etchant molecules and the polymer chains. PMMA, in particular, shows low resistance to alkaline etchants such as caustic potash and caustic soda, as well as to acidic etchants including nitric, sulphuric, and hydrofluoric acid. Although these substances can be used for chemical activation, their application in surface perforation is uncommon. The main reasons are their highly aggressive reactivity, significant health hazards that complicate handling, and their tendency to induce hairline cracks in the fiber surface during treatment [22, 23].In solvent-based treatments, the polymer surface is modified through dissolution, which disrupts the lattice energy and removes material. This approach produces a uniformly roughened surface, leading to smooth side-emission and good homogeneity [17, 24].

Thermal surface modification of fibers can be achieved either by laser ablation or by heated embossing methods. In laser ablation, a focused laser beam is directed at the fiber, causing localized heating that melts, decomposes, and evaporates the material. This process forms cavities that extend into the core and act as scattering elements [18, 25, 26]. The resulting cavity properties depend on parameters such as laser power, pulse duration, gas pressure, and the angle of incidence [27, 28]. In embossing processes, surface perforation is introduced through a discontinuous process using a heated perforated plate or a continuous process using a heated perforated roller. In both cases, the degree of surface modification depends on contact pressure, contact duration, surface structure, and embossing device temperature.

Bending Bends induce a displacement of the core–cladding interface, which can cause a light ray to drop below the critical angle, resulting in leakage of the guided light. Side emission can be induced by both microbends where the bending radius R is in the range of the fiber radius r or smaller, or macrobends with $R \gg r$ [29–32]. For large bending radii, this effect is negligible, but for small radii, bending losses become significant. While considered a disadvantage in data transmission, these losses can be exploited in sensing applications [33–35], or for creating light-emitting fabrics [36, 37]. The lateral emission of POFs caused by bending depends on different parameters, with the bending radius r_B and the fiber diameter d being the most critical. Increasing the bending radius decreases emission, while increasing the fiber diameter enhances it. There is no general rule for selecting an optimal bending radius, as it depends on multiple factors, including light source, desired brightness, illumination length and the fiber diameter. Below a certain critical radius, however, mechanical failure occurs. According to Wang et al., this critical bending radius can be estimated as [30]

$$r_{B,\mathrm{crit}} \geq \frac{d}{2 \cdot \varepsilon_Y} \tag{1.2}$$

where d is the fiber diameter and ε_Y is its yield elongation.

Luminescence Another approach is adding the luminescent materials into the fiber. Luminescent materials absorb the incoming light and re-emit it isotropically. In a polymer optical fiber, the re-emitted photons that meet the core–cladding boundary at angles above the critical angle satisfy total internal reflection and remain guided in the core. Photons emitted at smaller angles fail this condition and refract into the cladding, producing side emission. This approach allows for choosing the emission colour, which might be different from the incident light. By introducing different luminescent materials along the fiber, the emission colour can be varied spatially along its length [2, 12, 38, 39]. This method is commonly realized by incorporating photoluminescent dyes into the fiber, leading to so-called dye-doped POFs [39]. In comparison to scattering-based side-emitting fibers, luminescent POFs offer isotropic emission profiles [2, 39]. According to Stokes' rule, the emitted wavelength is longer than or equal to that of the excitation wavelength, which often results in a colour shift from blue to red The intensity and spectral properties of the fluorescence depend strongly on the absorption characteristics of the dye, its concentration, and the intensity of the coupled excitation light [39]. The wavelength of the emitted light depends on the photoluminescent dye used. In the visible range, emission can cover a wide spectral range, typically between 424 nm (violet) and 625 nm (red) [40]. Common dopants include organic dyes such as rhodamines (e.g., rhodamine B) [41] and nanomaterials like carbon or silicon quantum dots. The core, cladding, and photoluminescent dye must be compatible to allow co-processing. The dye should be uniformly dispersed within the core, and the core material must remain transparent at the emission wavelength of the dye [42].

From a fabrication point of view, luminescent POFs can be produced by several methods, such as polymerization of dye-doped monomers in fibre-shaped molds [43,44], wet-spinning of dye-doped polymer solutions [45, 46], co-extrusion or melt-spinning of dye-doped resins [47, 48], and heat drawing from dye-doped preforms [49, 50]. Among these, preform-based drawing is the most widely used, as it is compatible with large-scale optical fiber production [49–51]. In this process, a dye-doped preform with a core-cladding structure is prepared and then drawn into fibers in a fiber drawing tower, with the final fiber diameter controlled by the drawing speed [51]. These approaches enable the reliable production of luminescent POFs with tailored emission properties for both scientific and industrial applications [52].

Advantages and Limitations of Sidelight Activation Methods As outlined above, numerous techniques have been developed to induce lateral emission in POFs, each characterized by trade-offs in fabrication cost, process complexity, mechanical reliability, and

environmental footprint. Consequently, no single approach can be regarded as universally superior; rather, the selection of an appropriate method depends on the application and must balance requirements for durability, optical performance, economic feasibility, and sustainability [8].

The main advantage of bulk scattering approaches is that the side-emitting function can be incorporated directly during fiber fabrication, without additional post-processing steps. Both core and cladding doping allow good control of scattering intensity through the choice of particle material, concentration, and size. Additionally, doped fibers are durable and mechanically robust, since no external notches weaken the structure. Laser-induced volume modifications offer similar benefits with the added advantage of highly localized control of scattering density inside the core. However, bulk scattering methods have several limitations. Scattering particles and laser-induced voids permanently increase attenuation, and limits maximum usable fiber lengths and reducing optical efficiency. Particle addition also introduces material compatibility, dispersion, and recycling challenges especially when metal oxides or nanoparticles are used. In the case of laser-modified fibers, specialized equipment is required. Finally, doped fibers provide no post-production adjustability. Once fabricated, their sidelight power cannot be tuned without additional processing.

Surface perforation methods are highly flexible and allow any standard step-index POF to be converted into a side-emitting fiber. Abrasive (sandblasting), chemical, and thermal/laser treatments give control of lateral emission intensity, direction, and distribution. Because these treatments are applied after fiber manufacturing, fiber modification can be performed gradually by changing notch spacing, depth, or density along the fiber length. Laser ablation, in particular, offers precise and reproducible structuring, is compatible with both single fibers and woven textiles, and enables directional emission by shaping notches relative to the fiber axis. The major drawback of surface perforation is the mechanical damage to the fiber. Removal of material from the cladding weakens the fiber, reduces tensile strength, increases the risk of surface cracking, and may limit minimum bending radius or textile durability. Chemical treatments additionally pose safety and environmental concerns, produce hairline defects, and are harder to control uniformly. Abrasive and laser processes require careful parameter optimization to avoid cutting too deeply into the core, and most treatments introduce additional losses that limit usable fiber lengths. Furthermore, equipment costs vary widely: abrasive blasting is inexpensive while precision laser machining is costly.

Bending offers a unique advantage. lateral extraction is achieved without damaging the fiber at all. The effect arises naturally when POFs are integrated into textile structures, where many consecutive micro-bends decouple small fractions of light and together generate homo-

geneous illumination. Since the fiber remains intact, bending-based side emission preserves tensile strength, bendability, and lifetime better than surface-modified fibers. The approach is particularly well suited for large-area illumination (e.g., light-emitting fabrics). The primary limitation is lack of fine control: bending-induced emission depends on POF diameter, bend radius, weave structure, thread tension, and textile geometry, making output harder to tune precisely. Excessive bending creates inhomogeneous brightness and ultimately increases propagation losses, while too gentle weaving produces almost no emission. In addition, bending activation is generally constrained to textile systems and is impractical for standalone fibers or rigid installations.

Luminescent POFs offer unique advantages not achievable with scattering or notching. Fluorescent fibers produce exceptionally smooth, uniform side emission. These fibers can also provide wavelength conversion such as absorbing blue/UV light and emitting visible colors which enables specialized uses in sensing, medical illumination, and decorative textiles. On the other hand, luminescent methods introduce challenges related to dye compatibility and concentration control. Dyes can degrade over time leading to declining luminance. Incorporating dyes adds complexity to fiber processing, sometimes requiring specialized polymerization, melt spinning, or preform fabrication. Emission efficiency is strongly tied to excitation wavelength and input intensity, making output less predictable. Finally, luminescent fibers typically exhibit wavelength shift, meaning the output color depends on the dopant chemistry rather than the source which beneficial in sensing but limiting for white-light illumination applications.

1.3 THz waveguides

Lying between optical and microwave, THz waves cover the frequency range of 0.1–10 THz (wavelengths 30 μm to 3 mm) [53]. THz technology has emerged as a frontier field with unique capabilities for imaging, sensing and high-speed communications [54–57]. The development of THz systems relies on three main components: sources, detectors, and transmission lines. In comparison to the advancements in THz sources and detectors, the development of THz waveguides is still confined to theoretical studies and laboratory-scale research. This is primarily due to the strong absorption of THz waves in free space, especially by water vapour, which necessitates waveguide structures capable of isolating the guided mode from the external environment. Development of high-performance THz waveguides with low loss and low dispersion is essential for advancing next-generation THz systems. All proposed THz waveguides are based on metallic wires and dielectric waveguides which the guidance mechanisms of later one as conventional optical fibers can be categorized into the total internal reflec-

tion effect (TIR) [58], the modified total internal reflection (mTIR) [59]in microstructured fibers (or Photonic Crystal Fiber), the photonic bandgap effect (PBG) [60], the anti-resonant effect [61] and the topological channel effect [62].

Metallic waveguides with either rectangular or circular shapes are well used in microwave systems, but utilizing them in the THz range suffers from more loss as frequency increases [63]. Moreover, achieving flexible THz waveguides made only with metals is not possible. The solution is based on the design of metamaterial waveguides made of metal/dielectric coated waveguides [64]. Various types of metallic THz waveguides are shown in Fig. 1.2. The first successful experimental demonstration of a submillimeter circular metal waveguide in the THz range was shown by McGowan et. al [65]. The mentioned transmission line is limited by the high loss of the metal as well as group velocity dispersion of the guided waves. For overcoming these issues, Hadika et al [66] developed a flexible, hollow terahertz waveguide made of PVDF and compared the guidance properties of this waveguide with the same-sized metal waveguide. In order to meet the advantages of both metal and dielectric waveguides, hybrid-clad waveguides, also known as metamaterial waveguides, are introduced by Harrington et. al [67]

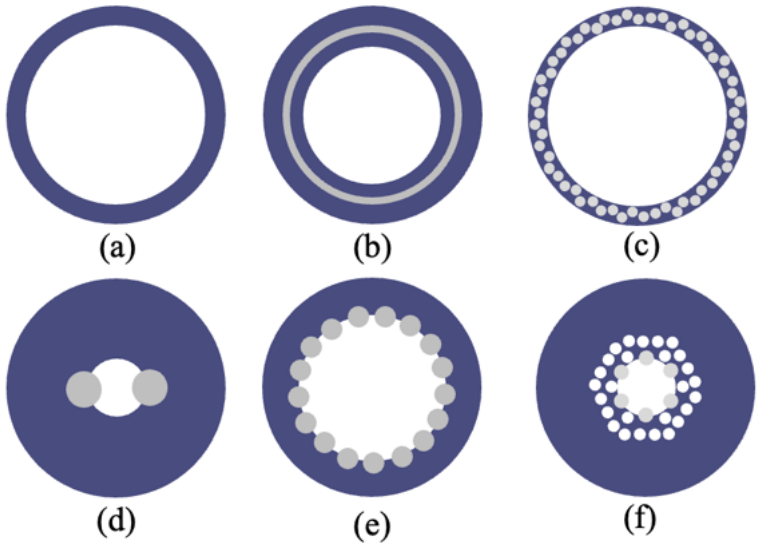

Figure 1.2 Metal-wire and coated hollow-core THz waveguides (a) Single metallic cladded waveguide, (b) hybrid cladded waveguide, (c) metamaterial cladding, (d) two-wire dielectric cladding, (e-f) cladding with multiple metal wire inclusions.

Another type of metamaterial waveguide is composed of a dielectric coating on metal. For

instance, when metal is coated with polystyrene, the dielectric layer enhances the effective reflectivity of the metal through interference effects, allowing the metal to function as a highly efficient mirror. Experimental studies on silver/polystyrene-coated hollow glass waveguides have demonstrated that this approach can significantly reduce transmission loss to about $0.95\,\frac{\mathrm{dB}}{\mathrm{m}}$, compared with the much higher loss values of 3.5–$5.0\,\frac{\mathrm{dB}}{\mathrm{m}}$ observed in uncoated metal waveguides [68, 69]. The important parameter is the thickness of the dielectric that should be optimized to obtain a low transmission loss in the desired frequency range. Another way of reducing loss is increasing the core size, but this increases the number of modes so that modal coupling and modal dispersion become problematic [64].

1.3.1 Characterization of Terahertz Waveguides

The two most used measurement systems for characterization of THz waveguides are terahertz time-domain spectroscopy (TDS) and THz continuous-wave (CW) spectroscopy. In THz-TDS, the coherent detection of the time-domain signal can directly measure the transient electric field. By applying a Fourier transform to this signal, the spectral response of the sample can be obtained.

CW-THz is another commonly used system for waveguide characterization. One of the advantages of the CW-THz system is the high spectral resolution that depends on the laser linewidth. Moreover, the full CW-THz system can be driven by laser diodes, which makes the system much more compact and less expensive in comparison to the TDS system [64].

In this work, the THz CW spectroscopy system (Toptica Photonics) is used for the characterization of copper waveguides. In this system, the radiation from two tunable distributed feedback (DFB) lasers operating at slightly different wavelengths in the infrared C-band was mixed. This signal was equally distributed to the emitter and detector arm using a 50:50 fiber coupler. Two photomixers are used as the emitter and detector. The first photomixer converted the mixed signal into THz radiation, while a second photomixer, together with a lock-in amplifier, was employed to detect the THz beam. A fiber stretcher in this CW-THz system is used to obtain the phase information. The configuration of the THz CW spectriscopy system is shown in Fig. 1.3.

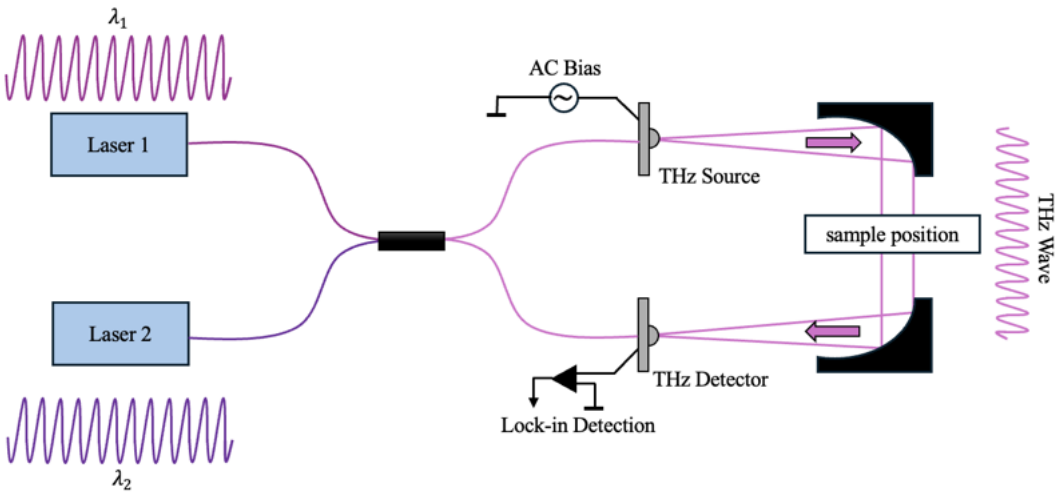

Figure 1.3 The schematic of the THz CW spectroscopy system. .

CHAPTER 2 METHODOLOGY

2.1 Theoretical Basis of Side Emission

Light propagation in side-emitting fibers can be modeled on a differential segment of length dz at axial position z (Fig. 2.1). Let $I(z)$ denote the guided optical power at position z, $A(z)$ the absorbed light power, and $S(z)$ the side-emitted power. Over $[z, z + dz]$, according to the energy conservation

$$I(z + dz) = I(z) - A(z)\,dz - S(z)\,dz. \tag{2.1}$$

$A(z) = \alpha \cdot I(z)$ where α is the constant material absorption coefficient. The side scattering effect is described by $S(z) = \delta(z) \cdot I(z)$ where $\delta(z)$ is the variable side scattering coefficient along the fiber length. Considering that the side scattering coefficient is composed of an intrinsic scattering coefficient δ_0 due to natural imperfections in the fiber core, and the extrinsic scattering coefficient $\Delta\delta(z)$ from the deliberate imperfections introduced either in the bulk or fiber surface. Therefore, the side scattering coefficient can be written as $\delta(z) = \delta_0 + \Delta\delta(z)$. Taking $dz \to 0$ in (2.1) yields

$$\frac{dI(z)}{dz} = -(\alpha + \delta(z)) \cdot I(z). \tag{2.2}$$

The design goal is to have a constant side emission along the fiber. If $\delta(z)$ is constant, then $I(z) = I_0 \cdot \exp[-z \cdot (\alpha + \delta)]$and $S(z) = \delta \cdot I(z)$ both decay exponentially; the emitted brightness is therefore non-uniform.

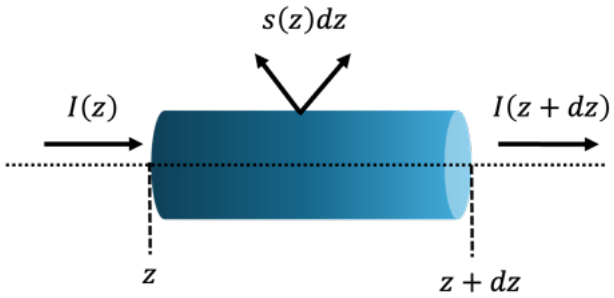

Figure 2.1 Light propagation in the side-emitting optical fiber.

A longitudinally uniform side emission is expressed by the condition

$$S(z) = S_0 = \text{const.} \tag{2.3}$$

This implies $\delta(z) = S_0/I(z)$. Substituting into (2.2) gives a linear differential equation

$$\frac{dI(z)}{dz} = -\alpha \cdot I(z) - S_0, \tag{2.4}$$

whose solution is

$$I(z) = \left(I_0 + \frac{S_0}{\alpha}\right) \cdot e^{-\alpha z} - \frac{S_0}{\alpha} \quad (\alpha > 0). \tag{2.5}$$

For weak absorption or short distances, this reduces to $I(z) \approx I_0 \cdot e^{-\alpha z} - S_0\, z$. The required extrinsic activation follows from $\delta(z) = \delta_0 + \Delta\delta(z) = S_0/I(z)$:

$$\Delta\delta(z) = \frac{S_0}{I(z)} - \delta_0. \tag{2.6}$$

A feasibility condition at the input is $\Delta\delta(0) \geq 0$, i.e.

$$\frac{S_0}{I_0} \geq \delta_0. \tag{2.7}$$

In the ideal lossless limit ($\alpha \to 0$) one has $I(z) = I_0 - S_0 z$, so $I(z) \geq 0$ implies $z \leq z_{\max} = I_0/S_0$. Evaluated at the threshold $S_0/I_0 = \delta_0$, the maximal uniformly emitting length becomes

$$z_{\max} = \frac{1}{\delta_0}. \tag{2.8}$$

Equations (2.2)–(2.8) summarize the general theory: constant δ leads to exponential, non-uniform emission; uniform brightness $S(z) = S_0$ fixes $\delta(z) = S_0/I(z)$; the guided power then follows (2.5); the necessary extrinsic activation is (2.6); and feasibility and length limits are set by (2.7) and (2.8).

Side emission from fibers designed for the maximal length. Consider fibers designed for uniform brightness with negligible absorption, $\alpha \ll \delta_0$. Let

$$L_{\max} = \frac{I_0}{S_0} \tag{2.9}$$

denote the length at which the guided power vanishes for the target constant side emission S_0. Using $S(z) = \delta(z)I(z)$ and $I(z) = I_0 - S_0 z$ in the lossless limit, the required extrinsic

activation is

$$\Delta\delta(z) = \frac{S_0}{I(z)} - \delta_0 = \frac{1}{L_{\max} - z} - \delta_0. \tag{2.10}$$

From the feasibility condition $S_0/I_0 \geq \delta_0$ it follows that $L_{\max} \leq 1/\delta_0$.

In fabrication, the implemented scatterer density may differ from the ideal profile (21) by an unknown multiplicative factor γ. A more realistic prescription is therefore

$$\Delta\delta(z) = \gamma\Big(\frac{1}{L_{\max} - z} - \delta_0\Big). \tag{2.11}$$

With $\delta(z) = \delta_0 + \Delta\delta(z)$, the power evolution obeys

$$\frac{dI}{dz} = -\Big(\delta_0 + \Delta\delta(z)\Big)\, I(z). \tag{2.12}$$

Solving (23) with $I(0) = I_0$ gives

$$I(z) = I_0\, e^{-z(1-\gamma)\delta_0}\Big(1 - \frac{z}{L_{\max}}\Big)^{\gamma}, \tag{2.13}$$

and the side-emitted power density follows as

$$S(z) = \delta(z)\, I(z) = S_0\, e^{-z(1-\gamma)\delta_0}\Big(1 - \frac{z}{L_{\max}}\Big)^{\gamma}\Big(\frac{\gamma}{1 - \frac{z}{L_{\max}}} + \delta_0(1-\gamma)\Big). \tag{2.14}$$

For such profiles $I(z) \to 0$ as $z \to L_{\max}$, consistent with the design objective.

2.2 Fiber Drawing Technique for Fabrication of Polymer Fibers

The fiber drawing process is a widely used technique for the fabrication of POFs in which a preform is drawn into fibers of different diameters. The preform can be a commercially available polymer rod or can be fabricated with the desired core–cladding geometry and material composition. The preform is then drawn into optical fibers in a fiber drawing tower. Most POFs can be drawn in relatively low temperatures, between 200 °C and 300 °C. An important step before starting the drawing process is degassing the preform to remove the air bubbles inside the polymer. Drawing a preform without degassing results in cracks and defects during the drawing. Degassing is done in an oven at a temperature below the polymer's degradation temperature for at least 2-3 weeks.

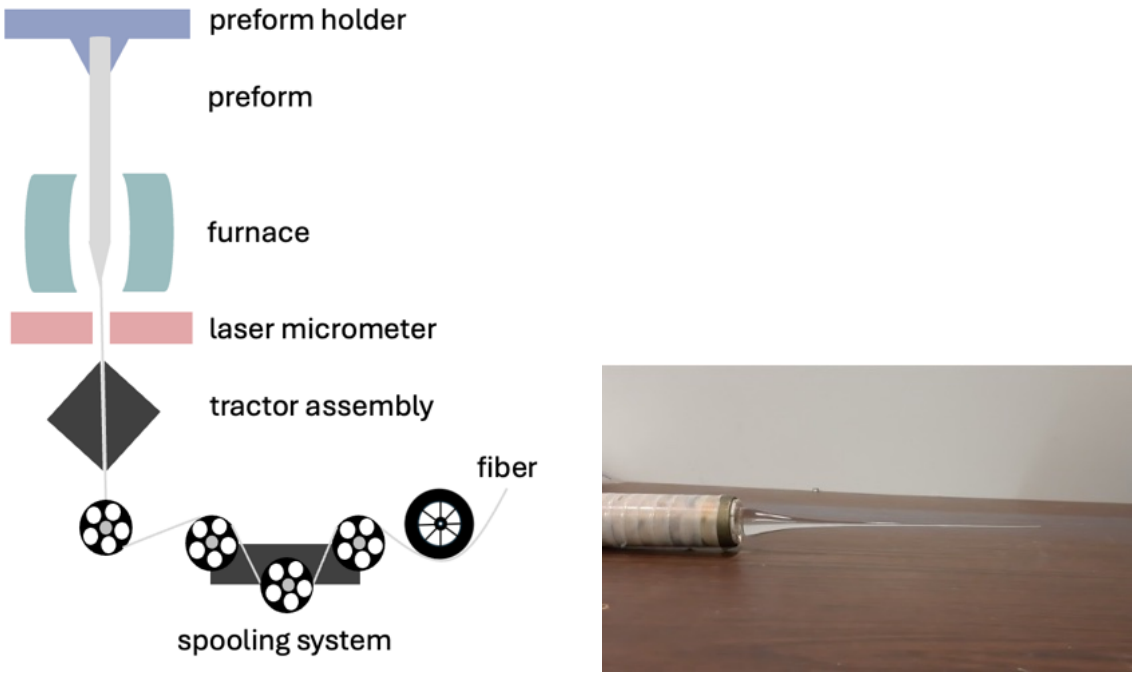

(a) (b)

Figure 2.2 Fiber drawing process: (a) schematic of the fabrication process; (b) photo of preform end after drawing.

During the drawing process, the preform is clamped inside a furnace and heated above its glass transition temperature but lower than its melting temperature. The schematic of the process is demonstrated in Fig 2.2a. The heating of the preform leads to a decrease of its viscosity, and the polymer goes from the solid state into a viscous state. In this viscous state, the take-up roll can draw the preform into a fiber. A critical condition during fiber drawing is the draw tension. It must be kept relatively low (typically 50–100 g). If the draw tension is too high, POF could be over-stretched and may shrink considerably and causing fiber deformation and optical loss [70].

2.3 Mode Analysis in Circular Metallic Waveguides

The transverse electric (TE) and transverse magnetic (TM) modes of a circular metallic waveguide are obtained as solutions of the wave equation in cylindrical coordinates. In particular, the TE modes correspond to solutions with $E_z = 0$, while the TM modes correspond to solutions with $H_z = 0$. These modes are defined by the cutoff wavenumber.

For circular metallic waveguides, the cutoff frequency is defined by the cutoff wave number

$k_{cnm} = \frac{p'_{nm}}{a}$, where n refers to the number of circumferential (ϕ) variations and m refers to the number of radial (ρ) variations [71].

The propagation constant of a mode is expressed as

$$\beta = \sqrt{k^2 - k_c^2}, \tag{2.15}$$

where

$$k = \omega\sqrt{\mu\epsilon} \tag{2.16}$$

is the free-space wavenumber in the medium, with μ and ϵ being the permeability and permittivity, respectively, and

$$k_c = \frac{p}{a} \tag{2.17}$$

is the cutoff wavenumber, where a is the waveguide radius and p represents either p'_{nm} or p_{nm}, which are the roots of the Bessel function and depending on the mode type.

For TE_{nm} modes, the propagation constant becomes

$$\beta_{nm} = \sqrt{k^2 - \left(\frac{p'_{nm}}{a}\right)^2}, \tag{2.18}$$

with cutoff frequency

$$f_{c,nm} = \frac{k_c}{2\pi\sqrt{\mu\epsilon}} = \frac{p'_{nm}}{2\pi a\sqrt{\mu\epsilon}}. \tag{2.19}$$

The first TE mode to propagate is the one with the smallest p'_{nm}, which is the TE_{11} mode. This mode is the dominant circular waveguide mode.

Similarly, for TM_{nm} modes, the propagation constant is

$$\beta_{nm} = \sqrt{k^2 - \left(\frac{p_{nm}}{a}\right)^2}, \tag{2.20}$$

with cutoff frequency

$$f_{c,nm} = \frac{k_c}{2\pi\sqrt{\mu\epsilon}} = \frac{p_{nm}}{2\pi a\sqrt{\mu\epsilon}}. \tag{2.21}$$

The first TM mode to propagate is the TM_{01} mode, with $p_{01} = 2.405$. Since this is larger than $p'_{11} = 1.841$ for the lowest-order TE_{11} mode, the TE_{11} mode is the dominant mode in a circular waveguide.

2.4 Experimental Methods for THz Waveguide Characterization.

2.4.1 The Knife-Edge Method

The knife-edge technique is a widely used method for measuring laser beam size. In this method, a sharp blade is translated transverse to the beam propagation axis, gradually obscuring the beam, while a detector measures the transmitted power as a function of the knife-edge position. As the blade moves across the beam, the detected power drops from the full beam power to nearly zero in an S-shaped curve. By analyzing this transmission curve, the beam's spatial intensity profile and diameter can be obtained [72]. In a typical setup, the knife-edge is mounted on a micrometre stage moving perpendicular to the beam. The blade is oriented so that it blocks one side of the beam. Initially, when the knife-edge is far to one side, the detector sees the full beam power. As the blade enters the beam, it progressively blocks the beam, causing the transmitted power to decrease. Finally, when the knife fully covers the beam, the transmitted power falls to essentially zero (aside from background or diffraction effects). The transition region of the transmission curve contains information about the beam's cross-sectional intensity distribution.

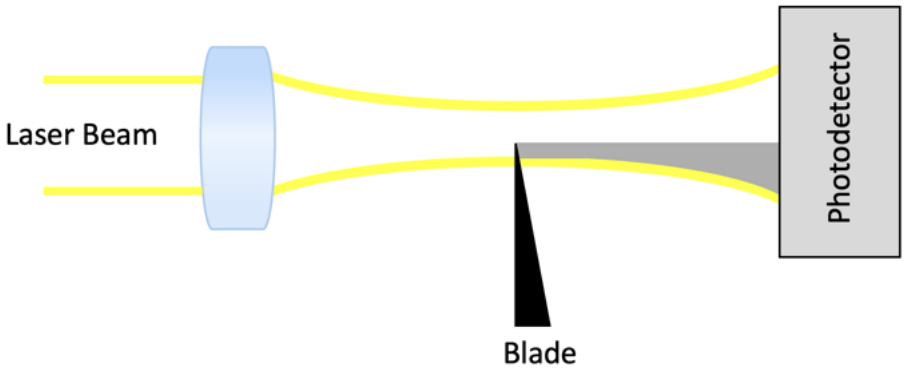

Figure 2.3 The schematic of the measurement of the laser beam radius using the knife-edge technique.

When scanning along the x direction, the transmitted energy at X is given by [72]:

$$\mathrm{E}(X) = E_0 \int_{-\infty}^{+\infty} \exp\left(-\frac{2y^2}{w_y^2}\right) dy \int_{-\infty}^{X} \exp\left(-\frac{2x^2}{w_x^2}\right) dx = E_0 w_y \sqrt{\frac{\pi}{2}} \left[\frac{1}{2} \int_{-X}^{X} \exp\left(-\frac{2x^2}{w_x^2}\right) dx + w_x \sqrt{\frac{\pi}{2}}\right] \tag{2.22}$$

By introducing the error function, this reduces to:

$$\mathrm{E}(X) = \frac{\pi}{4} w_x w_y E_0 \left[\mathrm{erf}\left(\frac{X\sqrt{2}}{w_x} \right) + 1 \right] \tag{2.23}$$

and the normalized knife-edge function is:

$$\mathrm{E}(X)_{\mathrm{norm}} = \frac{\mathrm{E}(X)}{\mathrm{E}(\infty)} = \frac{1}{2} \left[\mathrm{erf}\left(\frac{X\sqrt{2}}{w_x} \right) + 1 \right] \tag{2.24}$$

From this expression, the beam half-width w_x is determined as the distance between positions $X_1 = -w_x/2$ and $X_2 = w_x/2$ where the transmitted energy increases from 15.9% to 84.1% . This definition corresponds to the $1/e^2$ half-width parameter (Gaussian spot size).

After collecting the transmitted power as a function of the position, one approach to extract the beam radius is fitting the measured power vs. position data to a theoretical model. Curve fitting can be performed using several software including MATLAB.

2.4.2 Cutback Method

Attenuation in optical fibers is a critical factor influencing all fiber-based applications. Accurate characterization of fiber losses is essential for the design, implementation, and performance evaluation of optical systems. One approach for waveguide characterization is the cut-back technique. As illustrated in Fig. 2.4, the cutback method is used to measure the transmission loss of optical fibers at different lengths. The optical power transmitted along a fiber decreases exponentially with propagation distance and can be expressed as

$$P(z) = P_0 e^{-\alpha z} \tag{2.25}$$

where $P(z)$ is the transmitted power after a propagation distance z, P_0 is the input optical power, and α is the attenuation coefficient and considered to be uniform. In practice, α can be calculated by comparing the transmitted power measured at different fiber lengths. Considering the same coupling condition and if the same input power is coupled into the fiber, and the output powers P_1, P_2, and P_3 are measured for fiber lengths L_1, L_2, and L_3, respectively. The attenuation coefficient can be determined as [1]

$$\alpha = \frac{\ln\left(\frac{P_2}{P_1}\right)}{L_1 - L_2} \quad \text{or} \quad \alpha = \frac{\ln\left(\frac{P_3}{P_2}\right)}{L_2 - L_3}. \tag{2.26}$$

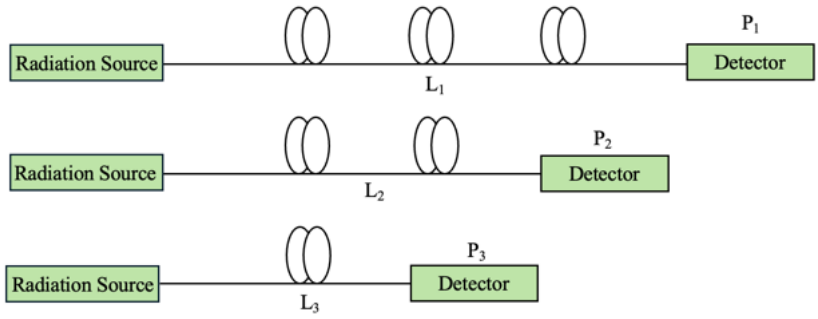

Figure 2.4 The schematic of the cutback process to measure attenuation of the fiber [1].

More generally, for any two arbitrary fiber lengths L_a and L_b with corresponding transmitted powers P_a and P_b, the attenuation coefficient can be expressed as

$$\alpha = \frac{\ln\left(\frac{P_b}{P_a}\right)}{L_a - L_b}. \tag{2.27}$$

This formulation allows the attenuation coefficient to be extracted directly from experimental measurements at different fiber lengths.

The extraction of the loss coefficient is based on fitting the measured transmission data to the exponential decay model. Taking the natural logarithm of the transmission relation gives

$$\ln P(L) = \ln P_0 - \alpha L, \tag{2.28}$$

which is a linear equation in L. Thus, plotting $\ln P(L)$ against L yields a straight line whose slope corresponds to the attenuation coefficient α. A MATLAB code was used to automate this procedure. The code uses the measured transmission spectra for all waveguide lengths, normalizes them to a reference signal, and fits the data to the exponential decay model. It estimates both the attenuation coefficient α as a function of frequency and the coupling spectrum.

CHAPTER 3 FABRICATION AND CHARACTERIZATION

3.1 Fabrication and Characterization of Polymer Fibers for Side Emission

We aimed to fabricate polymer optical fibers and subsequently modify them to achieve uniform side emission along their length. The development of such fibers requires precise control of scattering mechanisms. The fabrication process, surface modification techniques, and characterization methods employed to realize and evaluate side-emitting polymer fibers are presented in the first section of this chapter.

3.1.1 Fiber Fabrication Process

For the fabrication of side-emitting fibers, solid-core polymethyl methacrylate (PMMA) fibers were produced using the fiber drawing technique explained in 2.2. 1-inch PMMA rods were used as the preform, from which fibers with diameters ranging between 0.8 mm and 1.5 mm were drawn.

3.1.2 Realization of the Scattering Profile

In order to achieve uniform side emission along the fiber, it was necessary to determine the required scattering profile that governs how light leaks laterally as a function of propagation distance. From the theoretical analysis, it was found that the scattering coefficient, denoted as $\Delta\delta(z)$, must vary with the position z along the fiber in order to produce uniform emission.

The expression for the scattering coefficient can be written as:

$$\Delta\delta(z) = \frac{s_0}{I_0 e^{-\alpha z} - s_0 z} - \delta_0,$$

The side scattering coefficient must always be positive, which results in (a) an entrance condition at $z = 0$,

$$\Delta\delta(0) = \frac{s_0}{I_0} - \delta_0 \geq 0 \quad \Rightarrow \quad \frac{s_0}{I_0} \geq \delta_0 \tag{3.2}$$

and (b)

$$I_0 e^{-\alpha z} - s_0 z > 0. \tag{3.3}$$

The maximal length for which uniform emission can be sustained is therefore defined by the

equality

$$s_0\, z_{\max} = I_0 e^{-\alpha z_{\max}} \tag{3.4}$$

considering the low-absorption ($\alpha/\delta_0 \ll 1$), $e^{-\alpha z_{\max}} \approx 1$ and

$$z_{\max} \approx \frac{I_0}{s_0}. \tag{3.5}$$

If, in addition, the entrance condition is set to equality $s_0/I_0 = \delta_0$, this reduces to

$$z_{\max} \approx \frac{1}{\delta_0} = \frac{I_0}{s_0}. \tag{3.6}$$

Therefore, the scattering coefficient simplifies to:

$$\Delta\delta(z) = \frac{1}{z_{\max} - z} - \delta_0. \tag{3.7}$$

To generalize, a proportionality factor γ is introduced, leading to:

$$\Delta\delta(z) = \gamma \left(\frac{1}{z_{\max} - z} - \delta_0 \right). \tag{3.8}$$

Assuming that the concentration of scatterers $C(z)$ is proportional to the required scattering coefficient, we obtain:

$$C(z) = \gamma \left(\frac{1}{z_{\max} - z} - \frac{1}{z_{\max}} \right). \tag{3.9}$$

This formulation provides the theoretical basis for experimentally realizing the scattering profile. To translate it into practice, the fiber was divided into eight sections, each corresponding to a specific concentration of scatterers. The calculated distribution of scatterers along the fiber is summarized in Table 3.1, which lists the relative concentration in each section and the corresponding number of times the polishing paper was applied to the fiber surface.

Table 3.1 Calculated concentration of scatterers and corresponding number of polishing paper passes for each fiber section

Number of section	Concentration of scatterers: $C(z) = \gamma \frac{z}{L(L-z)}$	Number of polishing passes
1	$\gamma\left(\frac{1}{15}\right)$	2
2	$\gamma\left(\frac{3}{13}\right)$	7
3	$\gamma\left(\frac{5}{11}\right)$	14
4	$\gamma\left(\frac{7}{9}\right)$	23
5	$\gamma\left(\frac{9}{7}\right)$	39
6	$\gamma\left(\frac{11}{5}\right)$	66
7	$\gamma\left(\frac{13}{3}\right)$	130
8	15γ	450

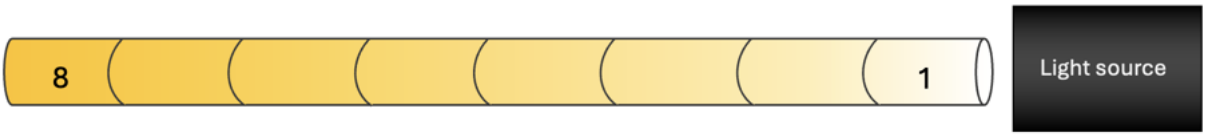

Figure 3.1 Schematic of fiber sections.

In order to enable lateral light emission, the fabricated fibers were subsequently modified to introduce scattering centers. This was achieved by scratching the fiber surface manually with a smooth abrasive paper. A 1-meter fiber segment was divided into eight equal sections, and in each section the polishing procedure was applied according to the calculated parameters summarized in Table 3.1. To ensure symmetrical modification, the polishing paper was applied to different sides of the fiber in a single direction. A schematic representation of the fiber divided into eight sections is shown in Fig. 3.1, where section 1 corresponds to the fiber input (nearest to the source) and section 8 corresponds to the fiber output.

a

b

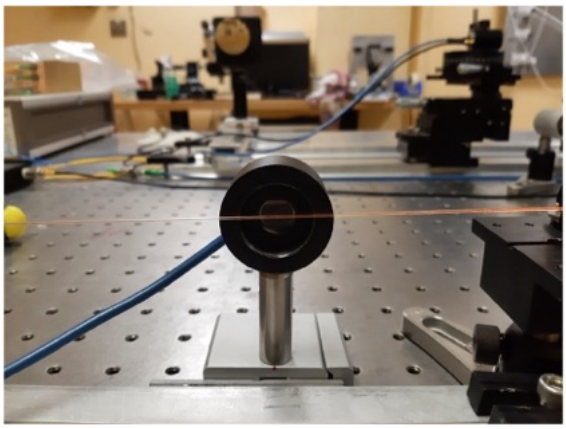

c

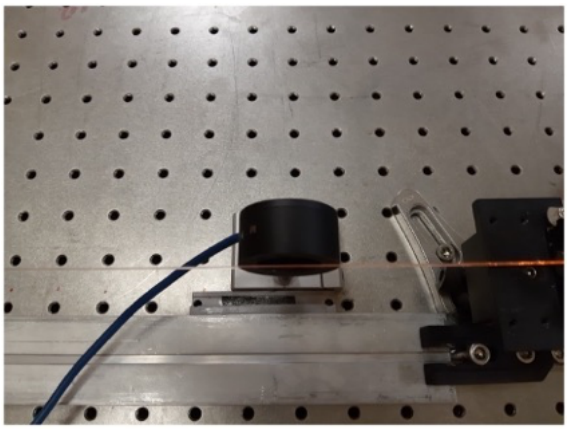

d

Figure 3.2 Images of SE-POF fabrication and measurement process. (a) PMMA fiber drawn on the fiber tower (b) Surface-modified fiber for side emission (c, d) The side-emission measurement setup

Following the modification, the side emission characteristics were evaluated. For this purpose, a supercontinuum light source was coupled into the fiber. The side-emitted light was measured using an optical power meter (Newport 841-PE Power/Energy Meter). The measurement setup is shown in Fig. 3.2c–d.

First, the background light intensity was measured with the supercontinuum source blocked, which was used as the reference signal. Subsequently, the side emission of a 1-meter-long fiber was recorded by sequentially rotating the fiber 90 ° and recording the emission from four sides. In each orientation, the emission was maximized at the fiber end before proceeding with the measurement in order to keep the coupling condition constant. The average intensity from these four orientations was then considered as the side emission intensity.

Despite the fabrication and surface modification process, the resulting side emission was not fully uniform along the fiber length. To identify the underlying reason of this non-uniformity, two possible limiting factors were evaluated:

1. **Material inherent loss:** If the polymer material exhibits a high intrinsic scattering coefficient δ_0, the available guided power decreases rapidly, making it difficult to sustain uniform emission over the entire fiber length.

2. **Realization of the scattering profile:** The theoretical analysis shows that a distribution of scatterers, given by 3.9 is required to achieve uniform side emission. However, in practice, the precise realization of this distribution is challenging, and deviations from the calculated profile lead to variations in emission intensity.

In the following sections, we analyze these two aspects in detail in order to clarify their contribution to the observed nonuniform side emission.

3.1.3 Characterization of Material Using the Cutback Technique

To evaluate the optical loss of the bulk material used for fiber fabrication, a cutback measurement was performed using four PMMA rods, each 30 cm in length. Before the experiment, the rods were polished to obtain flat end faces, ensuring proper optical contact. To minimize losses at the interfaces between rods, an acrylic index-matching gel (n = 1.4917, Cargille) was applied on the surfaces. The experimental setup, shown in Fig. 3.3, employed four mirrors to scan the input beam across the rod cross-section in two orthogonal directions, allowing excitation at 30 distinct launch points on the cross-section of the rod. Transmission was first measured with a single 30 cm rod, after which the second, third, and fourth rods were added sequentially, and the measurements were repeated under identical conditions. These measurements provide an estimate of the intrinsic material losses, which serve as a baseline for evaluating additional losses introduced during fiber drawing and surface modification.

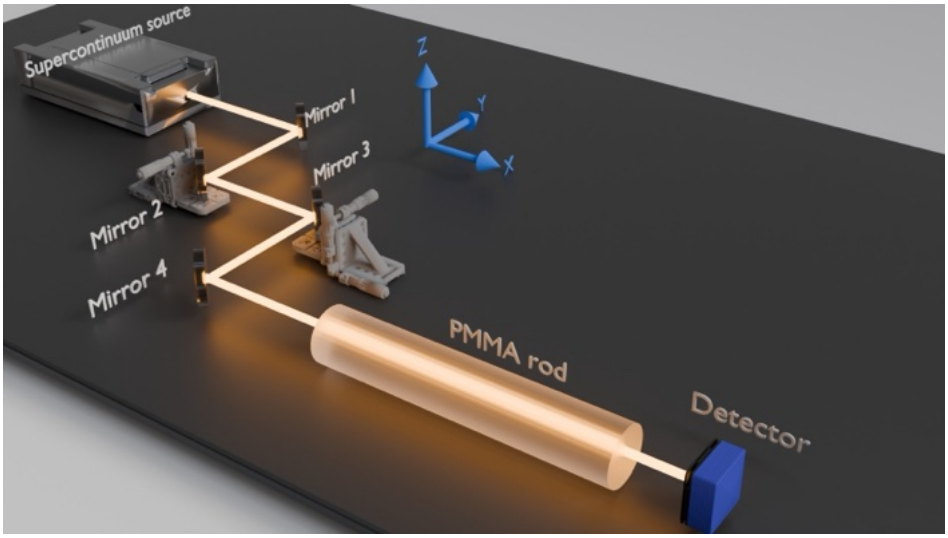

Figure 3.3 Schematic of the setup for the cutback measurement of PMMA rods.

3.1.4 Investigation of Scattering Profile

In addition to evaluating the intrinsic material losses, a series of measurements was performed in order to investigate how the scattering profile can be experimentally realized to achieve uniform side emission. For this purpose, a 30 cm long PMMA fiber was used. Initially, the side emission of the unmodified fiber was recorded and served as a reference. Subsequently, the fiber was progressively modified in seven steps by introducing surface scatterers through controlled scratching with polishing paper, and the side emission was measured after each modification step. This approach allowed us to monitor how incremental changes in the surface scattering profile affect the lateral emission distribution along the fiber length, thereby providing insight into how closely the experimental modifications could approximate the theoretically required profile.

To experimentally realize the theoretical scattering profile required for uniform side emission, several series of measurements were carried out using abrasive papers of various grit sizes. 50 and 25cm fibers were scratched using papers with grit sizes 240, 320, 400 and 600. The results showed that emission decreased after a certain number of scratches. This suggested that rough abrasive papers are too destructive, and smoother papers should be tested.

A 1-meter Fiber was then divided into four equal sections of about 25 cm each, and each section was scratched with abrasive paper with a grit size of 400. The number of scratches was gradually increased with distance from the source, fewer passes near the input, more passes toward the distal end, in order to compensate for the decrease of emission along the fiber. After this modification, the side-emission intensity was measured at 2.5 cm intervals along

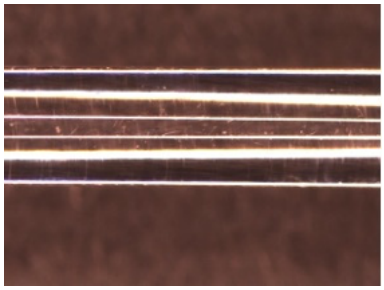

(a) PMMA fiber without any scratches

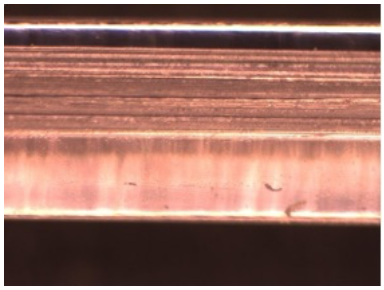

(b) PMMA fiber after 2 times scratching

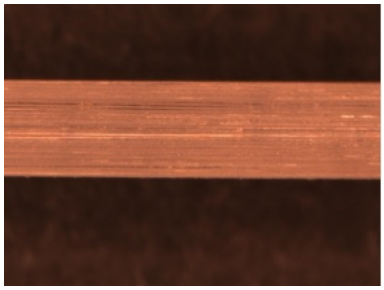

(c) PMMA fiber after 7 times scratching

Figure 3.4 Microscopic images of PMMA fiber surface modified using abrasive paper with grit size 240.

the fiber. The fiber was then flipped, and the measurement was repeated under identical conditions to check for directional dependence. A second round of scratching was applied to examine whether adding more passes would further enhance or instead reduce emission. In this case, one additional pass was made on the section closest to the source and two extra passes on the distal sections.

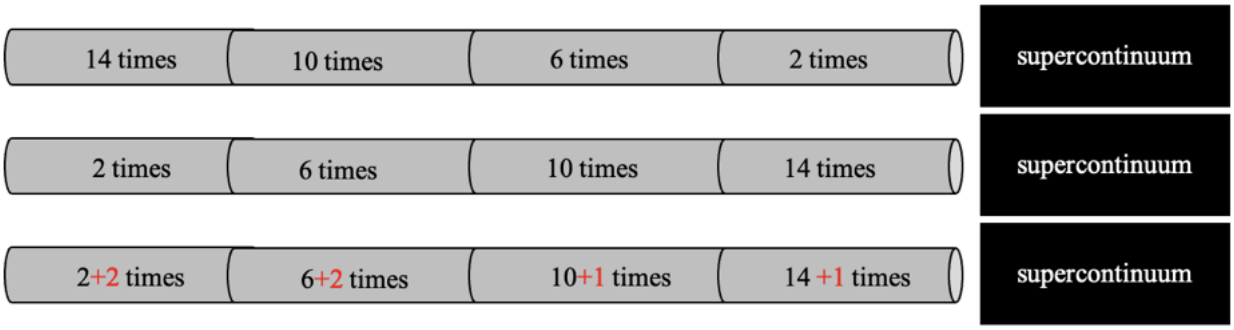

Figure 3.5 Schematic of scratching profiles applied to a PMMA fiber divided into four sections. Numbers indicate the number of longitudinal polishing passes per section. In the last profile, additional passes are shown in red. The fiber was flipped between measurements to assess directional effects.

An important observation was that the side-emission intensity was consistently higher at the boundaries between sections, i.e., at the points where each new scratching sequence was initiated. This effect is likely due to the way the polishing paper was first applied, i.e. pressed transversely at the boundaries before being moved along the fiber, creating a localized increase in scattering. This finding suggested that the orientation of scratching plays a significant role and motivated subsequent tests with modified scratching directions

where the scratching was applied transversely.

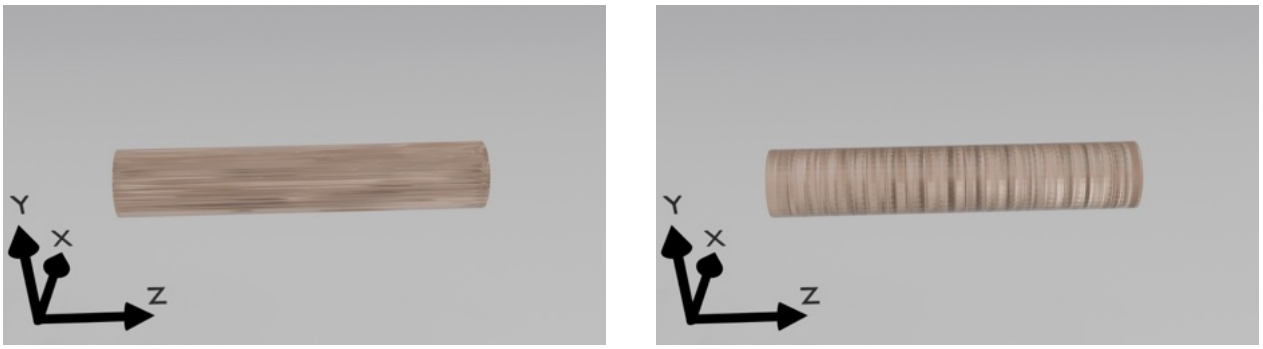

(a) (b)

Figure 3.6 Scratching direction: (a) longitudinal, (b) transverse.

As a first attempt to test this hypothesis, the experiment was repeated on a 30 cm fiber. The fiber was divided into two sections, and successive scratching profiles were applied using abrasive paper of grit sizes 400 and 240 as summarized in Table 3.2. In the first and second profiles, scratches were made uniformly along the entire fiber length. In the third profile, the fiber was divided into two halves, and only the section farthest from the source was scratched. In subsequent profiles, additional scratches were introduced on the second section: one pass with grit size 400 followed by one pass with grit size 240 in the fourth step, and finally, one more pass with grit size 240 in the fifth step. The results clearly demonstrated the effect of progressive surface modification. At step 4, it was not possible to carry out the measurement because light could no longer propagate through the fiber.

Table 3.2 Scratching profiles applied to a 30 cm PMMA fiber (diameter ∼1.6–1.7 mm) using abrasive papers of grit size 400 and 240.

Profile	**Description**
1st	Scratching along the entire fiber length with grit size 400.
2nd	Scratching along the entire fiber length with grit size 400 (repeated).
3rd	Fiber is divided into two sections; only the section far from the source is scratched with grit size 400.
4th	Second section scratched once with grit size 400, then once with grit size 240. The measurement was not possible at this step.
5th	Second section scratched once with grit size 240.

In the next step, a 20 cm PMMA fiber was tested in order to evaluate whether a more uniform emission profile could be achieved by combining different abrasive papers. The procedure

began with uniform scratching along the entire length using grit size 400. The fiber was then divided into two sections, and the distal section, farthest from the source, was selectively modified using grit sizes 240 and 120 in successive steps. To further refine the scattering distribution, additional localized passes with grit size 120 were applied between the last two sampling points. A summary of the profiles applied to the 20 cm fiber is given in Table 3.3. The results of the measurements will be discussed in chapter 4.

Table 3.3 Scratching profiles applied to a 20 cm PMMA fiber (diameter ∼1.6–1.7 mm) using different grit sizes.

Profile	**Description**
1st	Scratching along the entire fiber length with grit size 400.
2nd	Fiber is divided into two sections: the distal section (far from the source) is scratched with grit size 240.
3rd	Distal section scratched with grit size 120.
4th	Additional localized scratching between the last two sampling points with grit size 120.
5th	Repeated localized scratching between the last two sampling points with grit size 120.
6th	Further localized scratching between the last two sampling points with grit size 120.

3.1.5 Reflective Surface Design for Enhanced Light Collection

In a further step of this work, an integrating reflective surface was designed and fabricated in order to collect light uniformly from all sides of the fiber, therefore eliminating the need to rotate the fiber during measurements. The element was designed using SolidWorks and fabricated using an FDM 3D printing method, and its geometry was designed to enclose the fiber while redirecting side-emitted light toward the detector. To improve its optical performance, the inner surface was coated with a metallic spray, which provided a smoother and more reflective surface compared to the raw printed surface, although minor irregularities remained due to printing defects (Fig. 3.7).

Preliminary tests with this reflective surface demonstrated that it could enhance the detected side emission by efficiently gathering scattered light from the fiber. The efficiency of the integrating surface was calculated by comparing the detected power with and without the element. For a fiber length L, the efficiency $\eta(L)$ is defined as

$$\eta(L) = 10 \log_{10}\left(\frac{P_{\text{with}}(L)}{P_{\text{without}}(L)}\right), \tag{3.10}$$

where $P_{\text{with}}(L)$ and $P_{\text{without}}(L)$ are the measured powers recorded with and without the integrating surface, respectively.

However, the device was not incorporated into the main measurements, as the method required additional calibration to account for the effect of the integrating surface itself. At this stage, efforts were primarily focused on understanding and controlling the parameters that govern fiber emission through abrasive modification. However, such an integrating element could prove valuable in future work, as it offers a practical means to collect side-emitted light more effectively and may facilitate more reliable characterization of emission profiles.

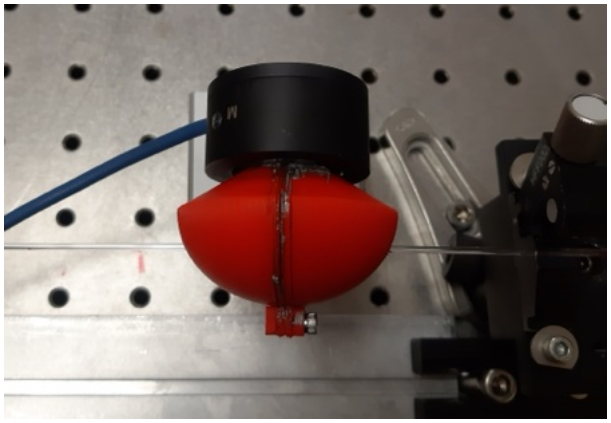

(a)

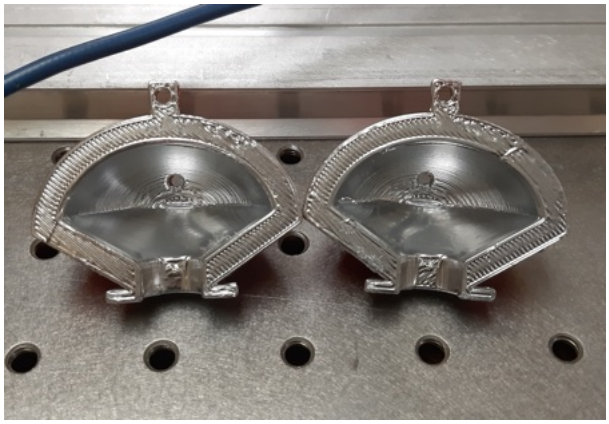

(b)

Figure 3.7 (a) A view of 3D-printed integrating element on the setup, (b) Inner surface of the integrating element with a metallic coating.

3.2 Characterization of Copper Waveguide

3.2.1 Calculation of Beam Size Using Knife-Edge Technique

To measure the beam size of the THz signal generated in the THz CW spectroscopy system, the knife-edge technique explained in 2.4.1 was employed. A metallic blade was mounted on two micrometre translation stage with a scanning range of 5 cm, allowing precise movement across the beam path. A schematic of the setup for beam size measurement is represented in Fig. 3.8.

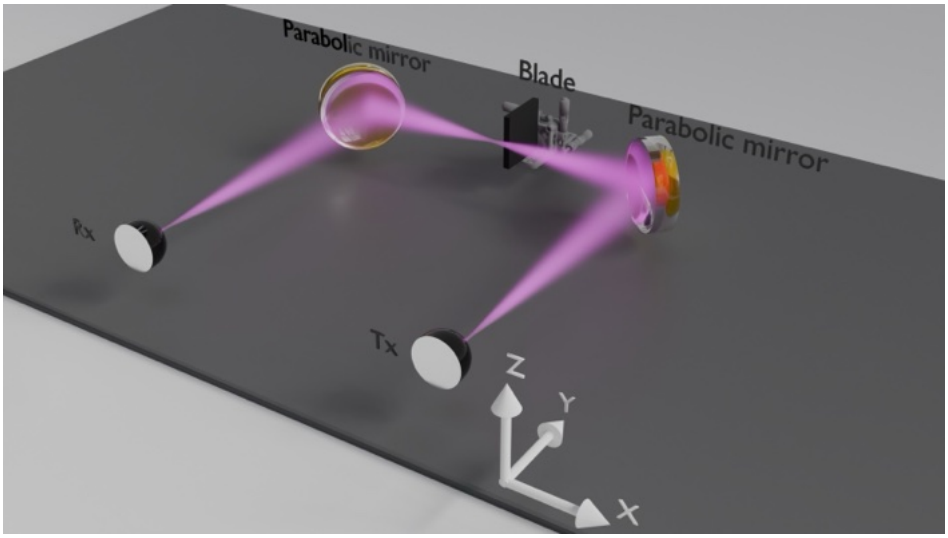

Figure 3.8 The schematic of the experimental setup for knife-edge measurement.

The blade was positioned at the midpoint of the setup where the beam waist was expected, and advanced through the beam in uniform steps of 5 mm. At each position, the transmitted signal was recorded across frequencies ranging from 100 GHz to 1 THz. This procedure enabled reconstruction of the beam profile by monitoring the reduction in transmitted power as the knife edge progressively blocked the beam. The primary motivation for this measurement was to determine the beam size in order to select appropriate PTFE lenses of proper size for the experimental setup. Knowledge of the beam diameter was essential to ensure that the chosen lenses would capture the full beam cross-section and properly focus it for subsequent experiments. For all measurements, background noise levels were recorded with the detector blocked, particularly at higher frequencies, to verify the signal. Examples of the obtained experimental data and the fitted curve are demonstrated in Fig.3.9. The recorded data at each frequency were processed in MATLAB. A Gaussian fit was applied to the measured transmission curve, and the derivative of the fit was used to calculate the full width at half maximum (FWHM).

The beam diameter D was then calculated using

$$D = \frac{2 \times \mathrm{FWHM}}{\sqrt{2 \ln 2}}.$$

This procedure allowed the calculation of the beam diameter at each frequency.

The results, summarized in Fig. 4.10.

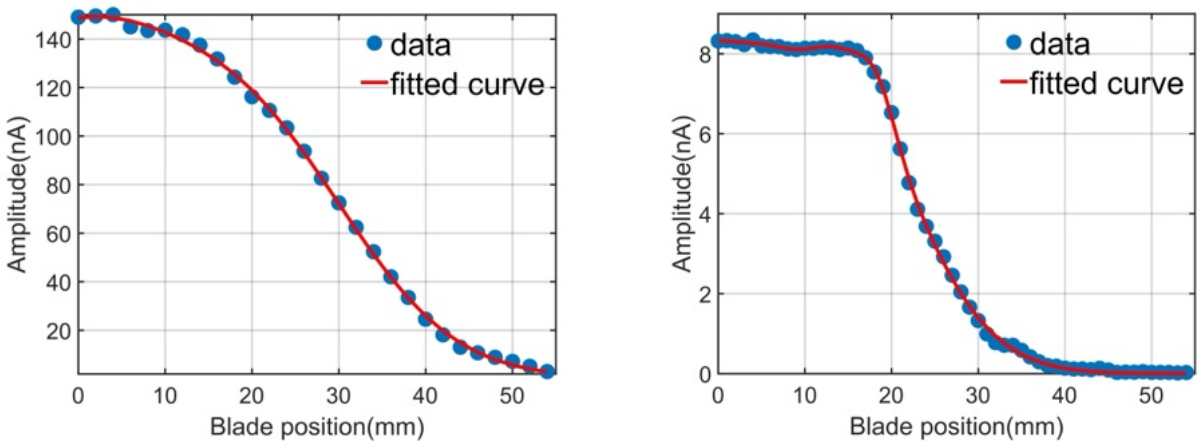

Figure 3.9 Examples of plots showing the experimentally collected data from knife-edge measurement (blue curve) and the theoretical fit (red curve) for frequencies of (a) 100 GHz, (b) 700 GHz.

3.2.2 Transmission Measurements of Copper Waveguides

To investigate the absorption losses of copper waveguides with 3mm inner diameter (ID) in the terahertz range, a cutback measurement was performed using three copper waveguides with lengths of 31 cm, 117 cm, and 204 cm. The schematic of the setup for these measurements is shown in Fig. 3.10 and the view of the experimental setup used for these measurements is shown in Fig. 3.12.

A homemade 3D-printed holder was used to mount the copper waveguides during the experiments. The holder was designed in SolidWorks and printed using a FDM 3d printer. The holder is designed in a way that, by unscrewing the upper pieces, a tube could be removed and replaced with another one without changing the other elements of the setup. This ensured the consistency of the coupling and outcoupling conditions during the measurements. The measurement procedure started with the alignment of the system. The first two photomixers and parabolic mirrors were aligned. After placing the first PTFE lens, the focal position of the beam was identified using an aperture and the holder was then positioned such that the beginning of the tube coincided with the position of the first aperture, while a second aperture was placed at the end of the holder. As shown in Fig.3.11a, the PTFE lenses were mounted on three miniature translation stages, allowing fine adjustment of their position to achieve optimized coupling and outcoupling conditions.

The coupling and outcoupling lenses were arranged so that both the entrance and exit of the

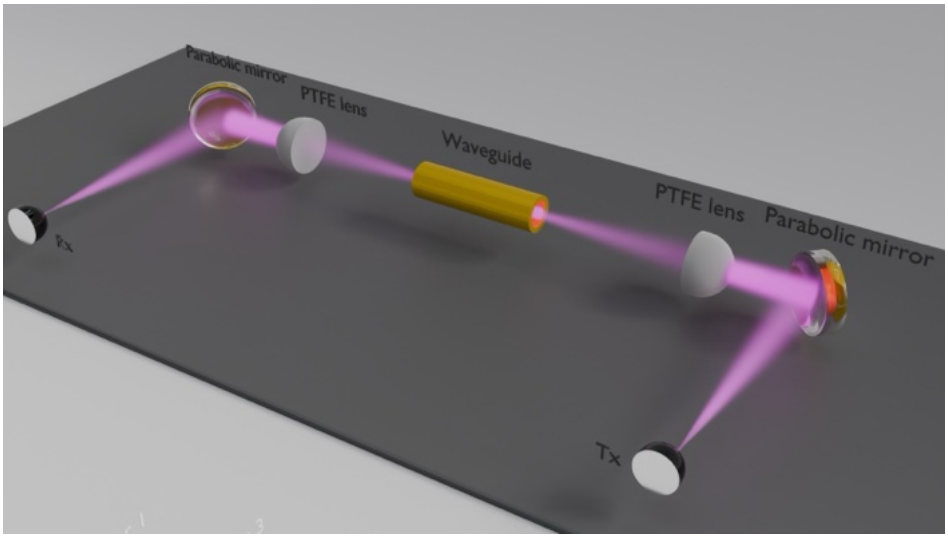

Figure 3.10 The schematic of the CW spectroscopy system for the transmission measurement.

tube were located at the focal planes of the lenses. To block the stray radiation, two large aluminum plates were placed around the apertures, ensuring that only the signal transmitted through the tube was detected (Fig.3.11b).

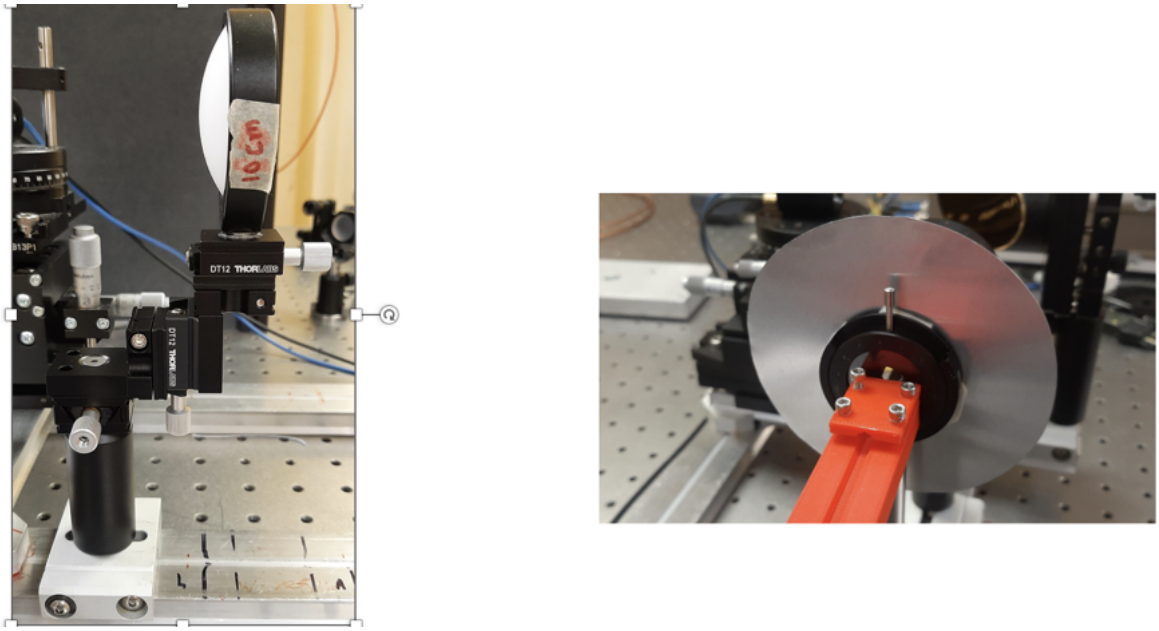

(a) (b)

Figure 3.11 Images of the experimental setup for characterization of copper waveguide.

After the alignment was completed, the straight copper tube was mounted in the holder, and

the coupling and outcoupling optics were adjusted to maximize the transmitted signal. Once this measurement was completed, the tube was removed by unscrewing the upper part of the holder and was replaced by the one-loop copper tube. The same coupling conditions were maintained, and only slight adjustments of the outcoupling lens, using the 3D translation stage underneath the lens, were applied to re-optimize the detected signal. In the next step, the one-loop tube was replaced with the two-loop copper tube following the same procedure. Finally, after all tube measurements were completed, the noise level of the system was recorded by removing the tube completely while leaving all other components of the setup unchanged. For each configuration—the straight tube, the one-loop tube, and the two-loop tube—the measurement was repeated with the tube flipped to examine possible asymmetry in coupling. All of these measurements were performed on the same day without turning off the system in order to minimize the influence of factors unrelated to the waveguides themselves. In this way, the effect of environmental variations such as temperature changes, as well as possible system instabilities including warm-up, electronic drift, or slight alignment shifts, was minimized. This ensured that any observed differences in the transmitted signal could be attributed to the copper waveguides and their geometry rather than external or system-induced variations.

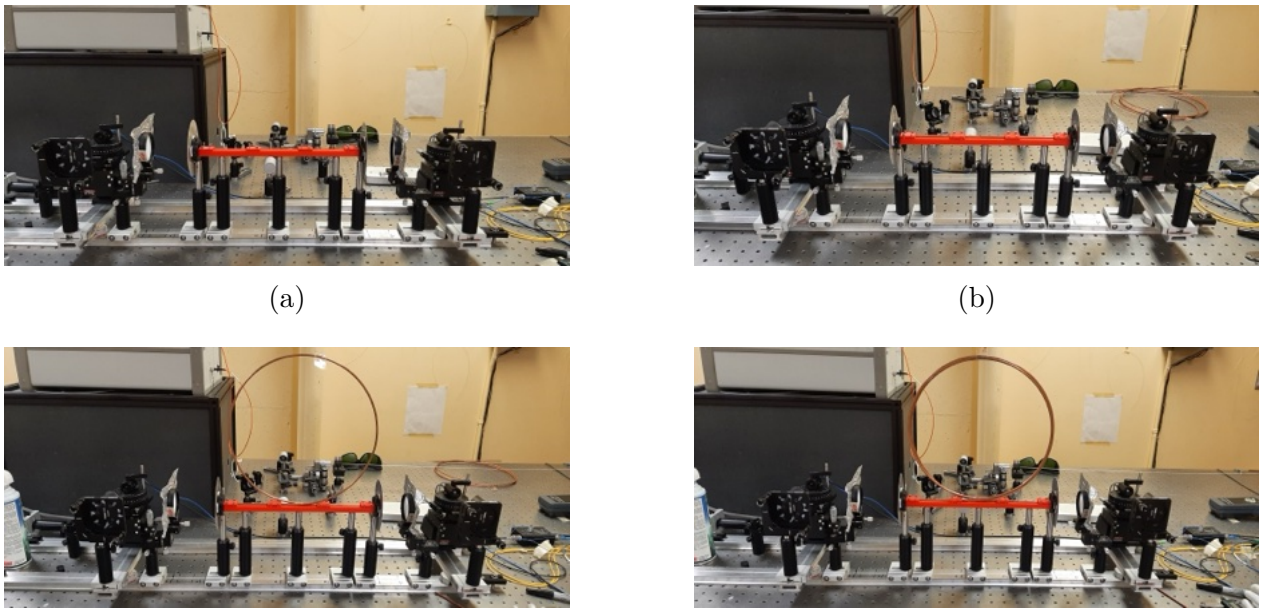

(a) (b)

(c) (d)

Figure 3.12 A view of the experimental setup for the measurement of (a) the reference signal, (b) the transmission of the straight copper waveguide, (c) the transmission of the one-loop copper waveguide, and (d) the transmission of the two-loop copper waveguide.

These experiments aimed to develop a consistent method to characterize the THz waveguides using the cutback technique. However, in practice, several issues were encountered. Despite maintaining the same alignment and coupling/outcoupling conditions, the transmitted signal was not consistent across repeated measurements. To investigate the reason for this inconsistency, several tests were performed. For example, the calibration of the system was checked, and different THz system parameters such as integration time and step size were varied to examine their influence on the measured signal. In another test, four plane mirrors were introduced into the setup to redirect the beam, allowing the signal to be monitored directly during the measurements without removing the waveguides or changing the lenses (Fig. 3.13). Mirrors 1 and 2 are kept on the setup during measurements, but mirrors 3 and 4 are removed each time and added again for the measurement. The purpose of this modification was to verify the stability of the detected signal throughout the measurement process. These tests confirmed that the difference in the signals is not related to the measurement system.

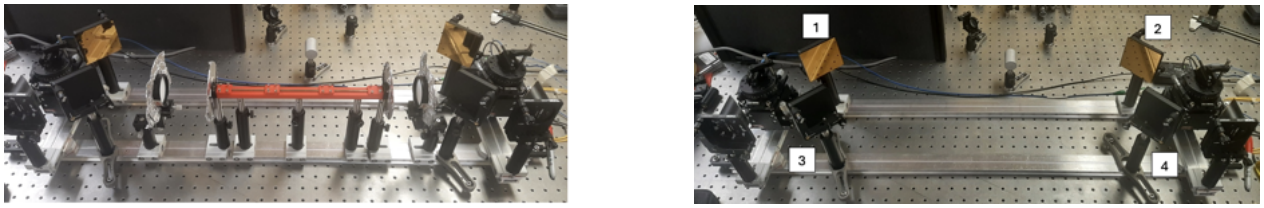

(a) (b)

Figure 3.13 A view of the modified experimental setup with four mirrors to verify signal stability during the measurements (a) empty system with mirrors (b) the measurement setup with holder.

Finally, the underlying cause was identified as the fact that the copper waveguides are multimode, and therefore the signal could not be coupled in a consistent way directly, without the use of an additional coupling element such as a taper to suppress higher-order modes. To confirm this assumption, the cutoff frequencies for several modes of the copper waveguide with a diameter of 3mm are calculated for TE (Table. 3.4) and TM (Table. 3.5) polarizations.

Table 3.4 Cutoff frequencies of TE modes of a 3-mm-diameter copper circular waveguide.

n	$\mathrm{TE}_{n1}(GHz)$	$\mathrm{TE}_{n2}(GHz)$	$\mathrm{TE}_{n3}(GHz)$
0	121.9763	223.3262	323.8485
1	58.6009	169.6910	271.7093
2	97.2118	213.4586	317.3550

Table 3.5 Cutoff frequencies of TM modes of a 3-mm-diameter copper circular waveguide.

n	$\mathrm{TM}_{n1}(GHz)$	$\mathrm{TM}_{n2}(GHz)$	$\mathrm{TM}_{n3}(GHz)$
0	76.5535	175.7071	275.4654
1	121.9763	223.3262	323.8485
2	163.4521	267.9214	369.8761

CHAPTER 4 RESULTS

4.1 Results on Side-Emitting Polymer Fibers

Fig. 4.1 presents the side-emission intensity measured along a 1 m PMMA fiber before and after surface modification. For the unmodified fiber, the emission is relatively lower along the entire length, with values gradually decreasing from the input toward the output. After the scratching procedure described in Chapter 3, a clear enhancement of side emission is observed across the fiber. In particular, the emission intensity near the input increases significantly, reaching values approximately two times higher than those of the unmodified fiber. However, despite this increase, the emission profile is non-uniform, with stronger scattering near the source and lower emission toward the distal end. This result confirms that surface modification by polishing can effectively increase side emission but also highlights the challenge of achieving a fully uniform distribution along the fiber length.

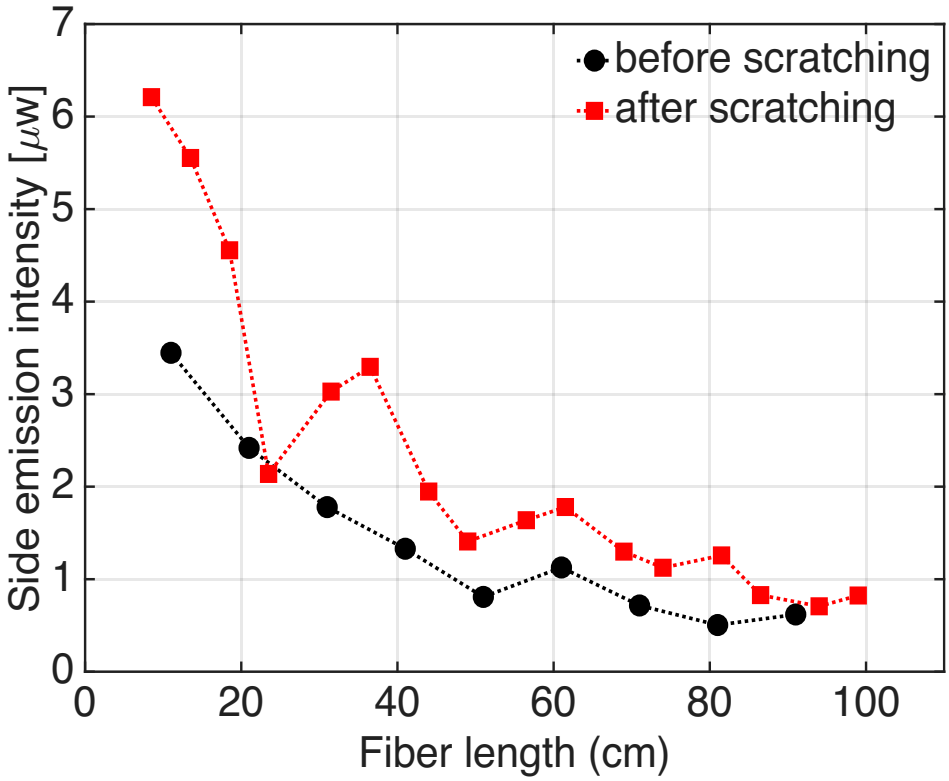

Figure 4.1 Side emission intensity of the PMMA fiber before and after surface modification.

To evaluate whether material absorption and scattering losses contributed to the observed non-uniform side emission, cutback measurements were performed on bulk PMMA rods.

Fig. 4.2 represents the transmission results obtained from the cutback measurement of the PMMA rods. Transmission values were recorded for rod lengths of 30 cm, 60 cm, 90 cm, and 120 cm, corresponding to one, two, three, and four rods, respectively. The data points were fitted with an exponential decay function in MATLAB to model the attenuation of light as a function of propagation length. From the fit, the material attenuation coefficient was extracted as $\alpha = 0.011 \pm 0.001\,\mathrm{cm}^{-1}$, indicating the intrinsic optical loss of the bulk PMMA material for fiber fabrication.

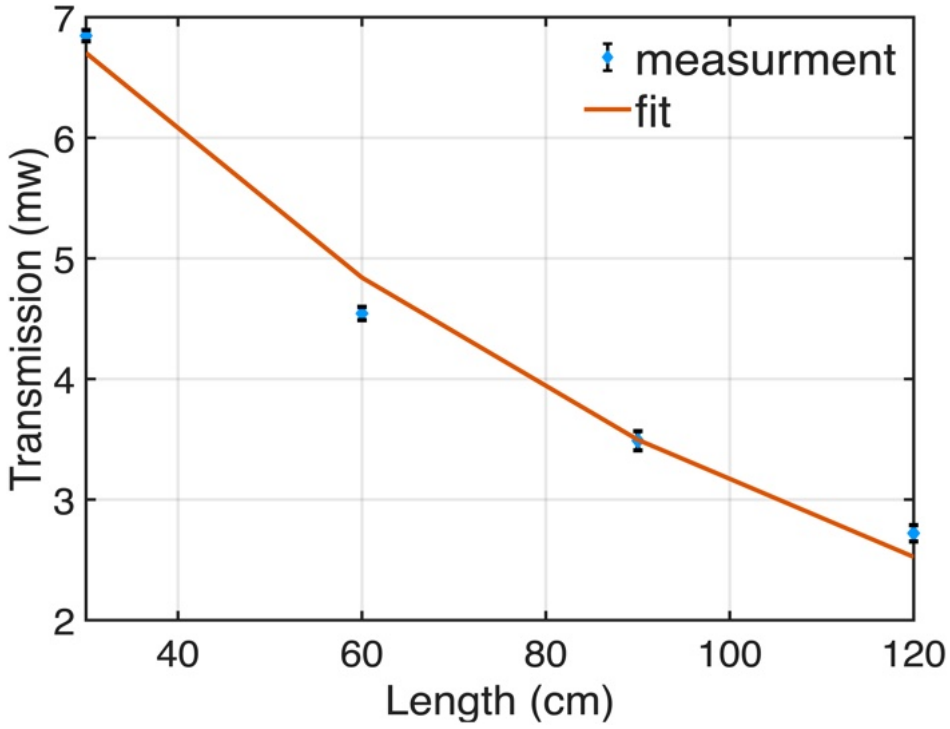

Figure 4.2 Transmission measurements of bulk PMMA rods with different lengths of 30 cm, 60 cm, 90 cm, and 120 cm. The experimental data points are shown with markers, and the exponential fit is shown as a solid line.

To investigate how the scattering profile can be experimentally realized, a 20 cm fiber was progressively modified, and after each scratching step, the side emission was recorded. The results are shown in Figure 4.3. The unmodified fiber exhibited very weak side emission across the measured length, consistent with the fact that, in the absence of scattering centers, most of the guided light remains confined to the core. After the first few scratching passes, the emission increased noticeably, particularly near the input end of the fiber. As the number of scratches increased, the side emission continued to increase, but the effect was not uniform along the length. Instead, localized regions of higher emission appeared. Beyond a certain threshold (e.g., 39–130 passes), the emission intensity decreased. This indicates that excessive

scratching degrades the guiding properties of the fiber and blocks the side light.

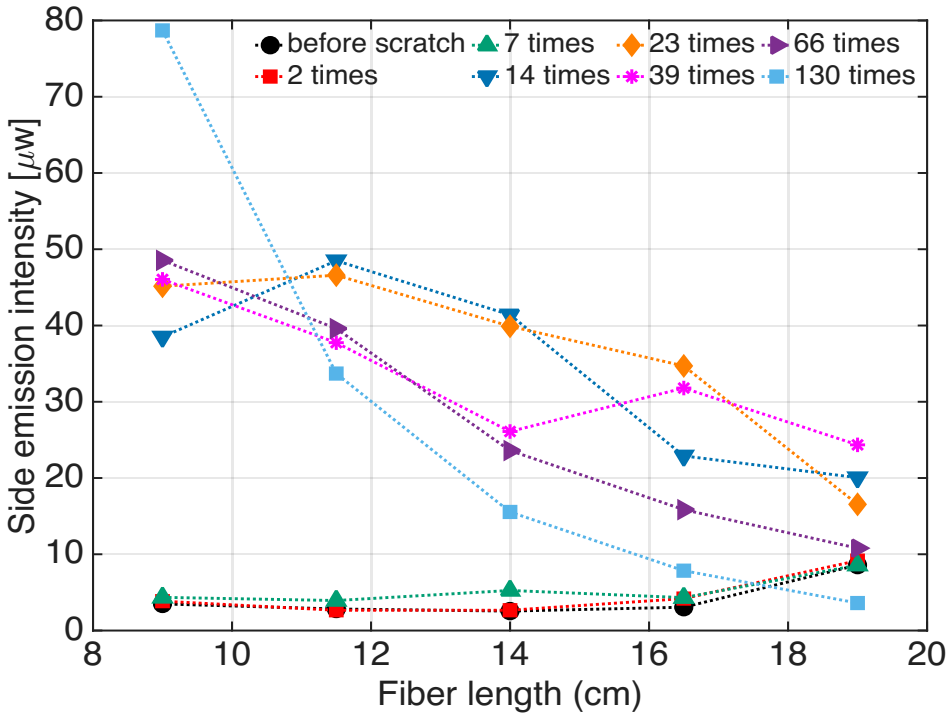

Figure 4.3 Side emission of PMMA fiber after modification for different numbers of passes with abrasive paper.

To further investigate how the scattering profile can be experimentally realized, fibers were modified with abrasive papers of different grit sizes, and the change in the side emission intensity was monitored as a function of the number of scratching passes. The results revealed a general pattern. After a small number of scratches, the side-emission intensity increased significantly, but beyond a certain threshold, further scratching became destructive and reduced the enhancement. At the beginning of the process, polishing introduces additional scattering centers on the fiber surface, thereby increasing side emission. With repeated scratching, however, the process either damages the surface, rendering it opaque, or smooths out the previously formed scatterers, reducing the emission. For grit size 240, a rough paper, as we can see in Fig. 4.4a, the emission increased sharply after only two passes, rising from 1 μW to 40 μW near the input of the fiber. However, after nine passes, the emission intensity decreased significantly, approaching values close to those of the unmodified fiber. This result demonstrates that very rough papers cannot be used for controlled enhancement.

For grit size 320 (Fig. 4.4b), the enhancement was more gradual. After two passes, the side emission increased and after nine passes, the emission remained at similar levels, in some regions even slightly higher. This indicates that, because grit 320 is smoother than 240,

more scratches could be tolerated before reaching the destructive effect. Nevertheless, after approximately twenty passes, the emission intensity decreased again.

For grit size 400, the side emission increases relative to the unmodified fiber but begins to decrease after the first two passes. Unlike the rougher papers with grit sizes of 240 and 320, however, the decay along the fiber is noticeably gentler and the intensity does not collapse as rapidly toward the distal end (see Fig. 4.4c). This indicates that grit size 400 creates a scattering profile that produces a more uniform emission along the fiber compared to the other papers. With additional passes (6, 10, 14), the overall intensity continues to decline, showing that too much scratching eventually damages the surface. The grit size 400 offers the best balance between enhancing emission and maintaining uniformity when the number of passes is kept limited.

For grit size 600, a smoother paper, the emission increased after two passes and appeared relatively uniform along the fiber. After six passes, the emission decreased, and with further scratching to 10, 14, and 18 passes, it changed only slightly (Fig. 4.4d). This indicates that with a smooth paper, it is difficult to create new effective scatterers; extra passes mostly smooth the surface rather than strengthening scattering.

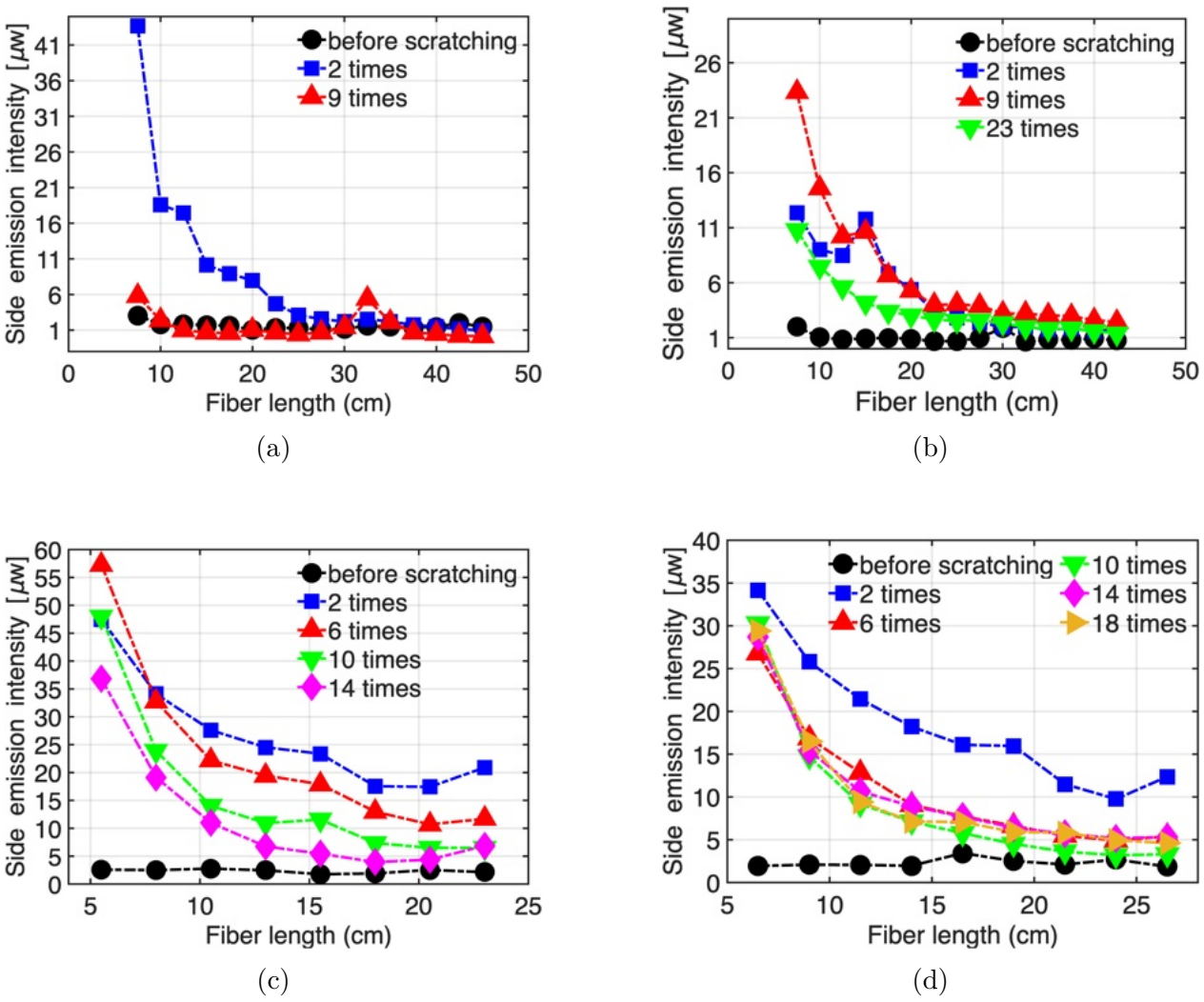

Figure 4.4 Comparison of side emission intensity of PMMA fibers modified using abrasive papers with various grit sizes. (a) Grit size 240. (b) Grit size 320. (c) Grit size 400, and (d) Grit size 600.

To conclude the series of comparative tests with different grit sizes, abrasive paper with a grit size of 400 was selected for further investigation, as we observed a partial uniformity and relatively higher enhancement in side emission using this abrasive paper. In this experiment, a 1-meter PMMA fiber was divided into four sections. Each section was scratched with fewer scratches applied near the input end and more scratches toward the distal end, aiming to compensate for the natural decrease of emission intensity along the fiber length. To evaluate possible directional effects, the fiber was flipped and remeasured under identical conditions. The emission profiles obtained before and after flipping were nearly identical, indicating that the side emission was not strongly dependent on fiber orientation and that

the scattering centers were distributed consistently along the modified surface. A second round of scratching, in which additional passes were applied to each section, was also tested. The results show that this additional modification did not significantly influence the emission profile, suggesting that the first scratching sequence had already established the dominant scattering distribution. Beyond this point, further abrasion appeared to contribute little to the overall emission and, in some regions, even slightly reduced the intensity, indicating the beginning of surface degradation.

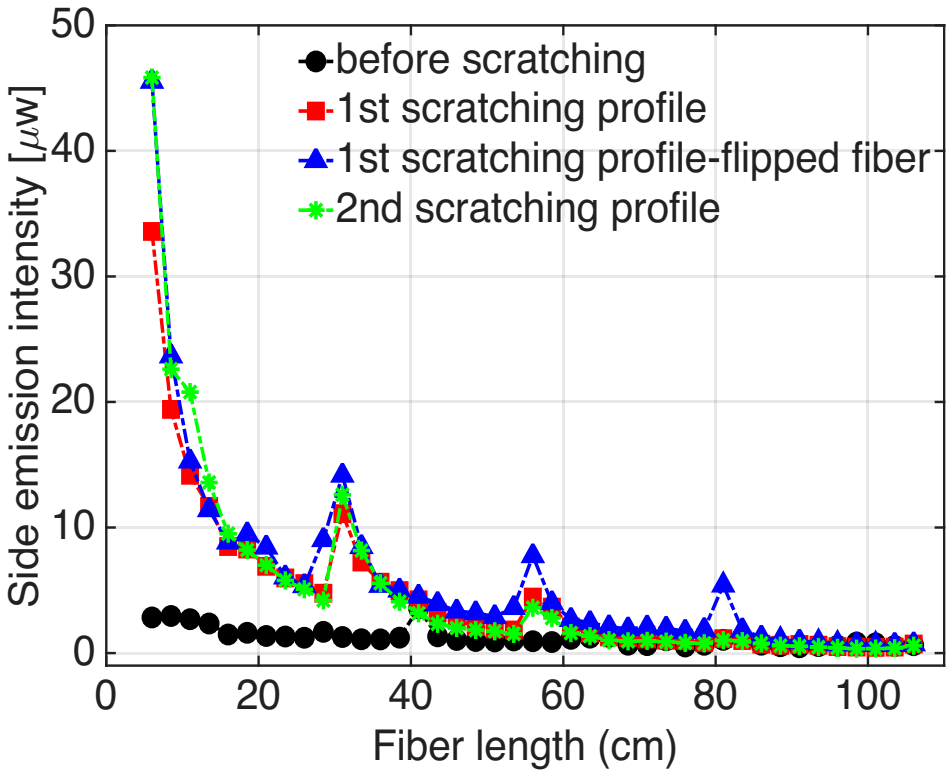

Figure 4.5 Side-emission intensity of a PMMA fiber after multiple surface-modification steps with abrasive paper with grit 400.

From the previous measurement, we understood that transverse scratching might help in enhancing the emission more effectively than longitudinal scratching. To test this idea, we performed additional modifications using transverse scratching profiles. The emission followed the same general trend. It increased after the first profile. With the second profile, emission at the beginning of the fiber was further enhanced, but a decrease was already noticeable in the far sections, indicating that the effect was not uniform. When the third scratching profile was introduced, where additional transverse scratches were applied to the far section of the fiber, the emission intensity dropped sharply across much of the fiber, showing that the abrasion disrupted transmission rather than enhancing scattering. In the

fourth profile, the excessive roughening prevented light from propagating along the fiber, and emission was almost completely blocked. As shown in Fig 4.6a, the emission is concentrated at the first section, while the rest of the fiber remains dark. This indicates that the scratches introduced at this stage block the lateral emission. After applying one additional scratch with abrasive paper of grit size 240, side emission could again be observed in the second section of the fiber. As shown in Fig 4.6b, light was successfully launched and guided along the fiber, with visible emission extending from the input region toward the far section. The result is shown in Fig.4.7.

(a) Side emission blocked after excessive scratching.

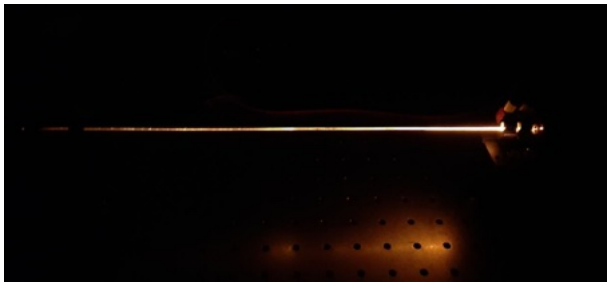

(b) Side emission restored in the second section after scratching with grit size 240.

Figure 4.6 Comparison of side emission before and after additional scratching with rougher abrasive paper.

This indicates that, although excessive roughening in the previous step had hindered transmission, using a rougher paper appeared to produce more scattering centers and restore the emission, consequently. The observation suggests that combining different grit sizes can influence the emission.

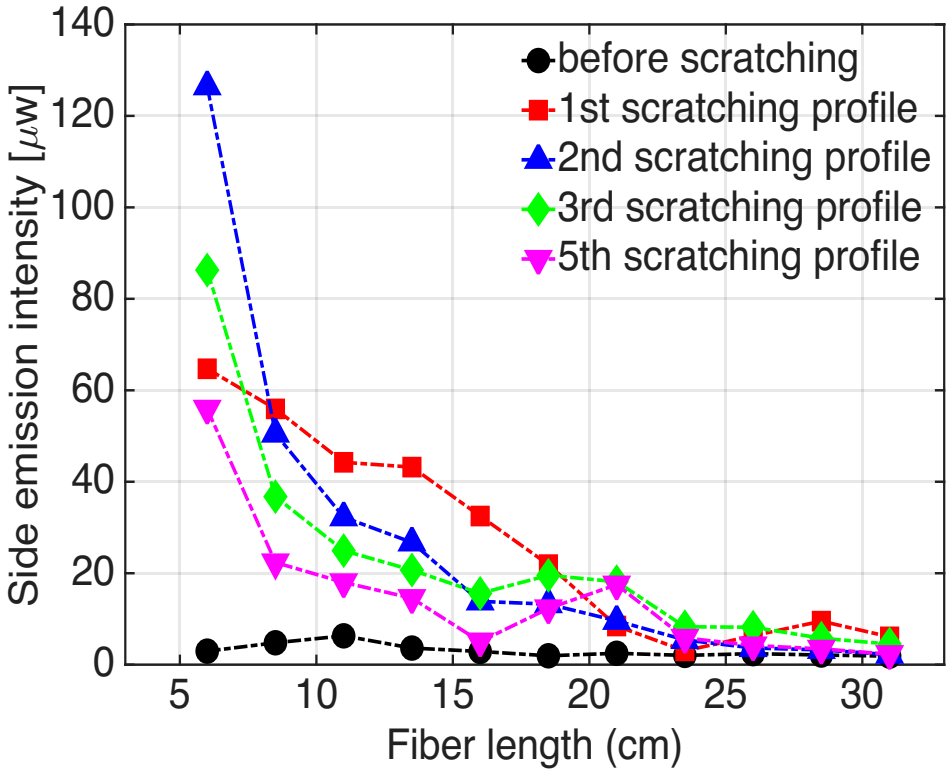

Figure 4.7 Side emission intensity of PMMA fiber after transverse scratching.

In the previous experiment, excessive scratching eventually blocked light propagation, but a subsequent pass with a rougher paper restored side emission by reintroducing effective scatterers. Motivated by this, we tested whether applying successive polishing steps with different grit sizes could both raise the emission level and reduce transmission loss, giving a more uniform emission profile. A 20 cm PMMA fiber was modified in stages, starting with grit 400 and then adding passes with grits 240 and 120. The results (Fig. 4.8) followed our expectation: the first profile clearly enhanced the side emission, and the second profile further improved it. After the third profile, the emission decreased, indicating the beginning of surface degradation. With additional profiles, the response fluctuated, and by the sixth profile the emission rose sharply to $\sim$ 90 μW, nearly twice the peak values achieved when using grit 400 ($\sim$40–50 μW). Thus, combining grit sizes can overcome the saturation and blocking behaviour seen with a single abrasive and can drive the emission beyond the previous maximum.

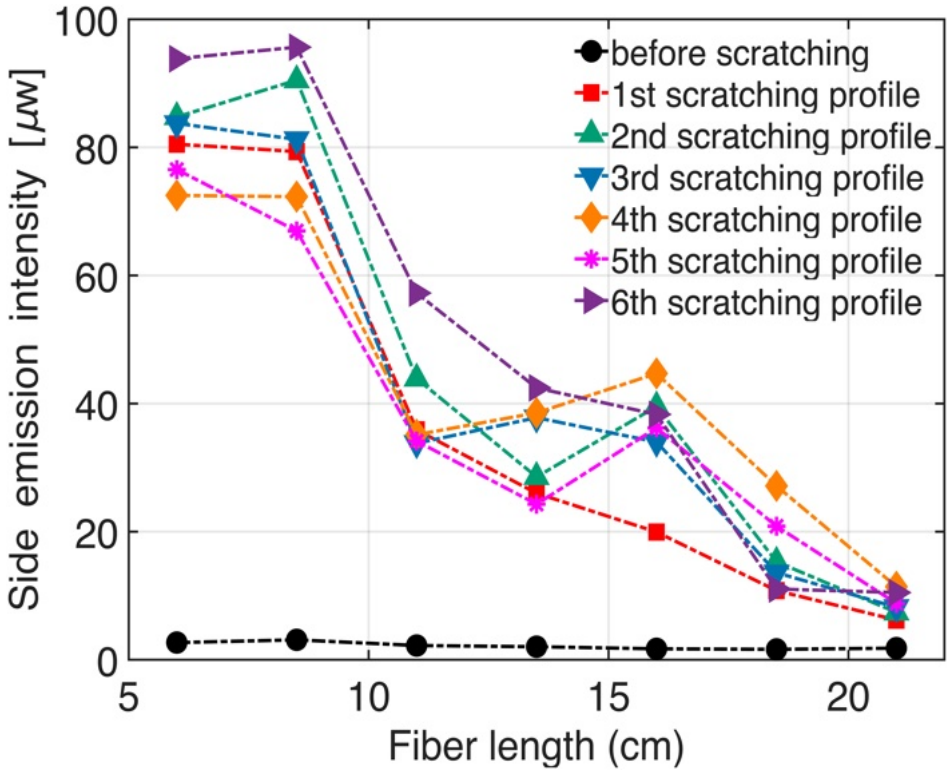

Figure 4.8 Side emission intensity of PMMA fiber after several modification sequences.

Using abrasive papers can reliably enhance side emission, but a single grit size tends to saturate and then damage the surface with continued passes. A combination of grit sizes, initiating scattering with a smoother paper and then following with rougher papers, can recover and further increase emission after degradation. Nevertheless, the approach remains only partly controllable. Emission varies with the position on the fiber relative to the source, and uniformity along the fiber is not completely achieved.

Fig. 4.9 compares the side emission intensity measured with and without the integrating reflective surface. It is evident that the integrating surface increased the detected emission along the fiber. At the fiber input, the recorded intensity rose from approximately 6 μW without the surface to nearly 9 μW with the surface. Over the first half of the fiber, the integrating element increases the signal by up to ~ 3 dB which is equivalent to approximately doubling the collected optical power, representing a clear enhancement in collected light. This confirms that the reflective coating effectively gathers the scattered light toward the detector. These results highlight that such an integrating surface can be used to facilitate measurements by eliminating the need to rotate the fiber during the measurement. Despite its potential, this element was not incorporated into the main sets of measurements because calibration was necessary to separate the contribution of the reflective element from the

intrinsic emission of the fiber. Without fully understanding the emission mechanisms of the fiber, it was not possible to introduce additional components into the measurement procedure. The focus of this work, therefore, remained on controlling emission through surface modification alone. Future studies may benefit from employing such an integrating surface for the ease of measurements and for the potential development of a more consistent measurement method.

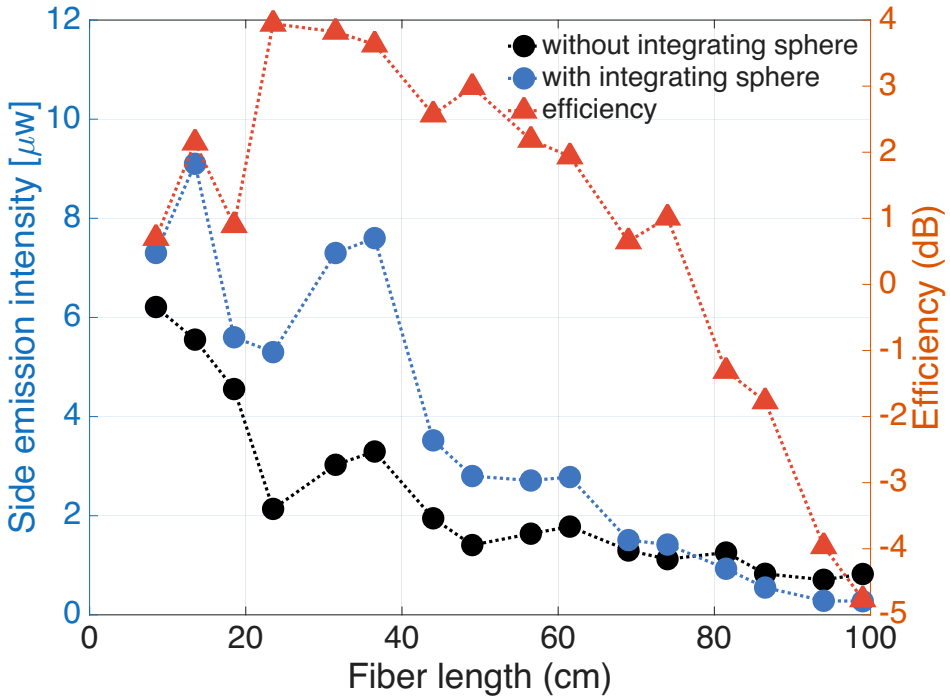

Figure 4.9 Comparison of side-emission intensity measured along a 1-meter PMMA fiber with and without the use of the integrating sphere.

4.2 Results on Copper Waveguide Characterization

The calculated beam diameters for different THz frequencies are presented in Fig. 4.10. The calculated beam diameter, obtained from repeated measurements to ensure reliability, shows a frequency-dependent behaviour. The beam diameter varies across the frequency range, with values from approximately 55 mm at 100 GHz to about 18 mm near 500 GHz. Based on these results, the choice of components for the experimental setup was made to ensure efficient collection and focusing of the beam. In particular, a 2-inch PTFE lens was selected, as its aperture covers the majority of the measured beam sizes across the investigated frequency range.

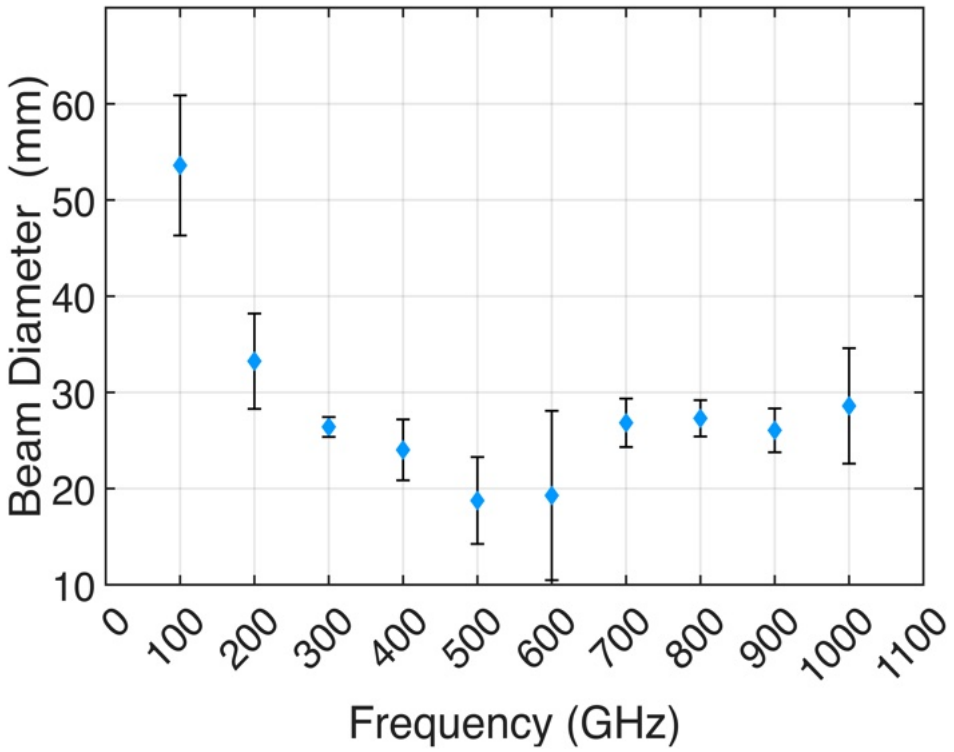

Figure 4.10 Beam diameter as a function of frequency, measured at different positions using the knife-edge method.

Fig. 4.11 presents the recorded transmission spectra of the 3-mm-diameter copper waveguides of different lengths alongside the noise level of the system, as well as the extracted attenuation using the cutback analysis. As shown in Fig. 4.11a, the transmitted signal decreases with increasing waveguide length, with the two-turn (204 cm) waveguide exhibiting the strongest attenuation compared to the straight (31 cm) and one-turn (117 cm) configurations. The comparison with the noise level confirms that the measured spectra are well above the system noise within most of the investigated frequency range. The corresponding frequency-dependent attenuation is shown in Fig. 4.11b. The extracted loss values remain relatively low at lower frequencies but gradually increase with frequency, reaching more than 15 dB/m at around 1 THz.

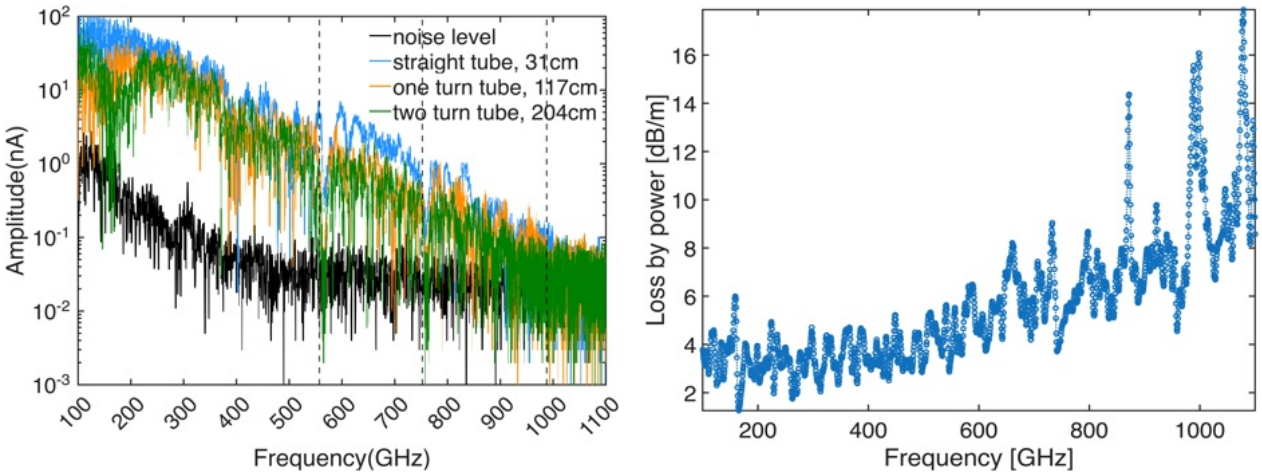

(a) (b)

Figure 4.11 (a) Transmission spectra of a 3-mm-diameter copper waveguide: straight (31 cm), one-loop (117 cm), and two-loop (204 cm), compared with the noise level of the system. (b) attenuation of the 3-mm-diameter copper waveguide as a function of frequency.

These results of measurement and calculation demonstrate that the method can be effectively used to extract the attenuation characteristics of hollow-core waveguides. To verify the reliability of the loss extraction method, multiple measurements were performed. Fig. 4.12 and Fig. 4.13 compare transmission spectra obtained from three of the measurements for the straight, one-loop, and two-loop copper waveguides.

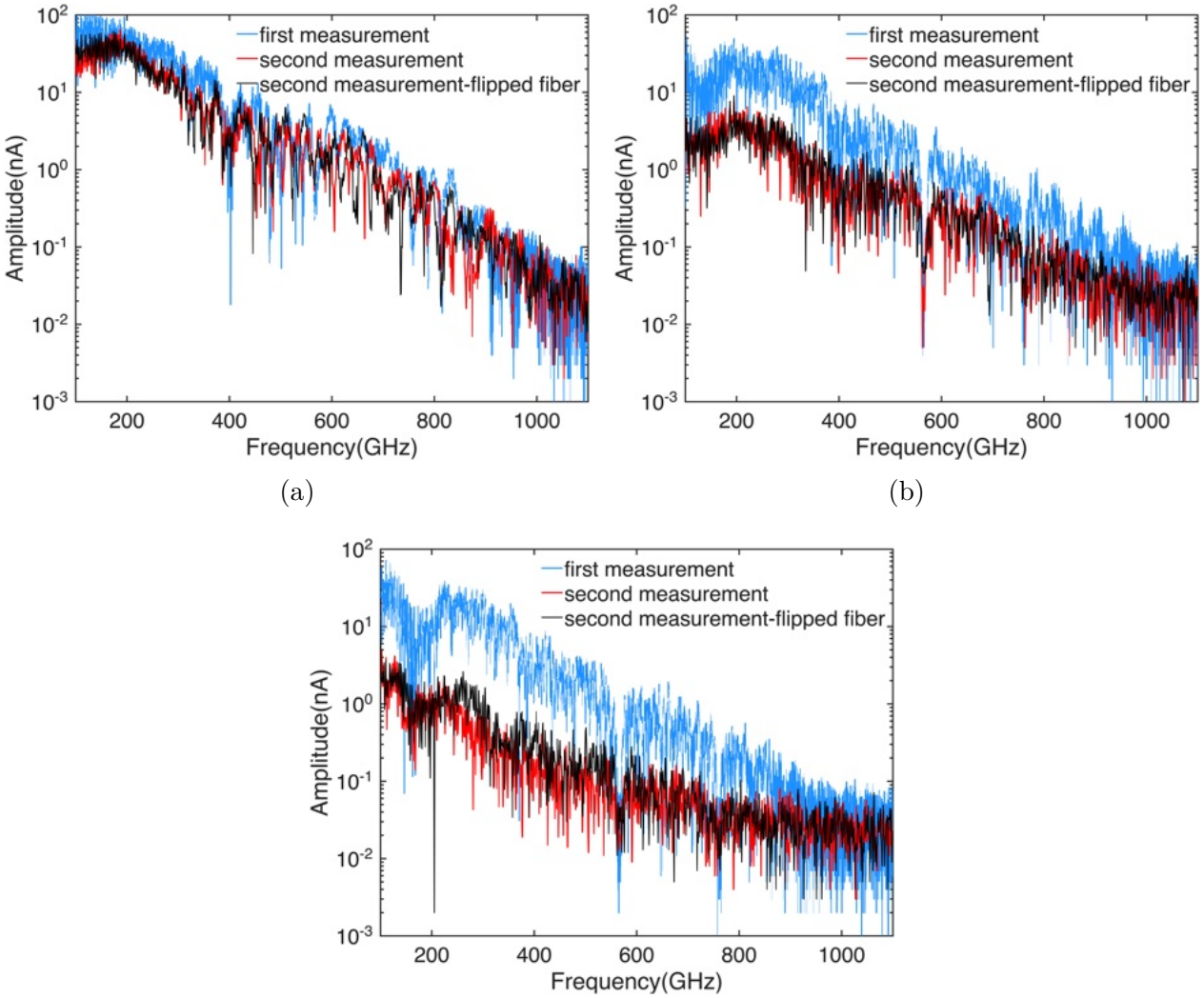

Figure 4.12 Comparison of signals from measurements one and two (a) Straight waveguide, (b) One-loop waveguide, (c) Two-loop waveguide.

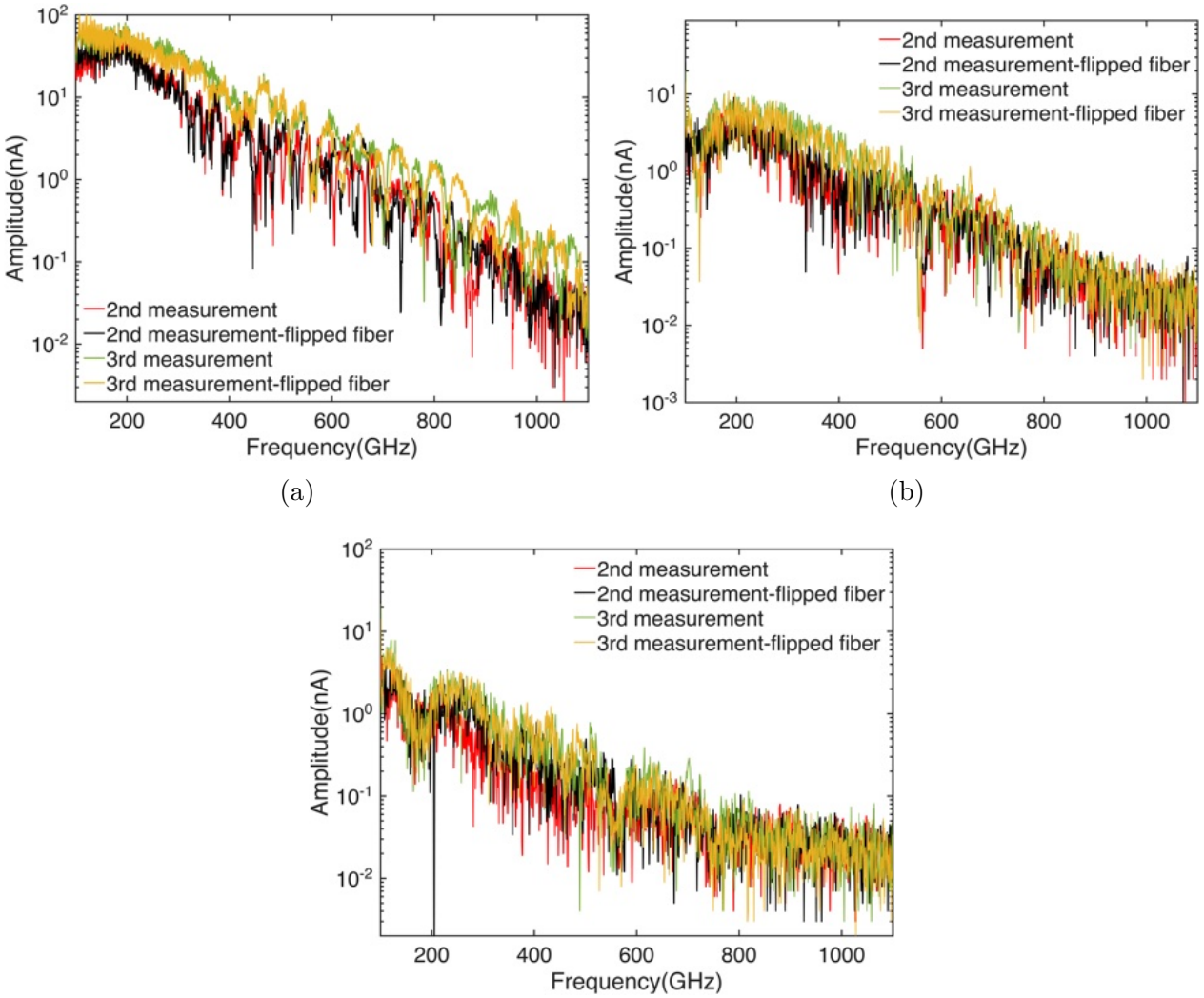

Figure 4.13 comparison of signals from measurements two and three (a) Straight waveguide, (b) One-loop waveguide, (c) Two-loop waveguide.

The results show clear differences between the recorded signals. This variability indicates that the transmission response is not fully reproducible across different experiments. To further illustrate this, Fig. 4.14 shows the average transmission spectra for the three waveguide configurations, with shaded regions representing the standard deviation (std) across the performed measurements. These plots confirm that the signal varies significantly from one measurement to another, leading to large deviations in the extracted loss values.

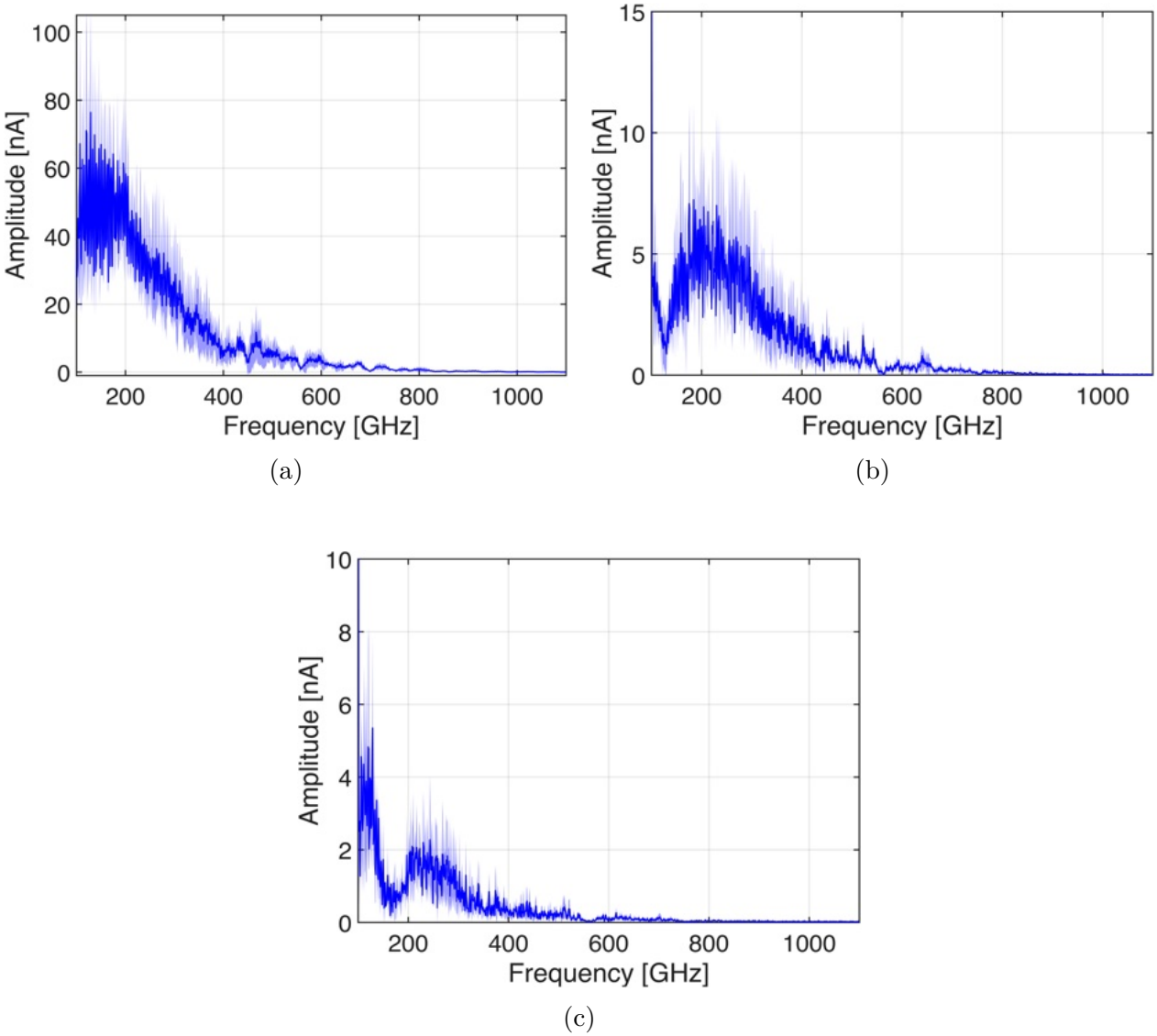

Figure 4.14 Average transmission spectra with the standard deviation for copper waveguides (a) straight waveguide, (b) one-loop waveguide, and (c) two-loop waveguide. The shaded regions represent the standard deviation across multiple measurements.

Since the extracted values of attenuation showed noticeable deviations across different measurements, the stability of the system itself was questioned. To verify whether the variations originated from the measurement setup, a stability test was carried out. In this test, the signal path was redirected using four flat mirrors to allow repeated measurements under identical conditions, without changing the main setup. The spectra from the system were recorded once during the measurement and once at the end of the measurement. The results of this stability test are presented in Fig. 4.15. This result indicates that the system remains stable over time and the warming effects or environmental factors do not significantly affect the measured signal. This confirms that the observed inconsistencies in attenuation values do not arise from the measurement setup, but instead are related to the properties of the waveguides.

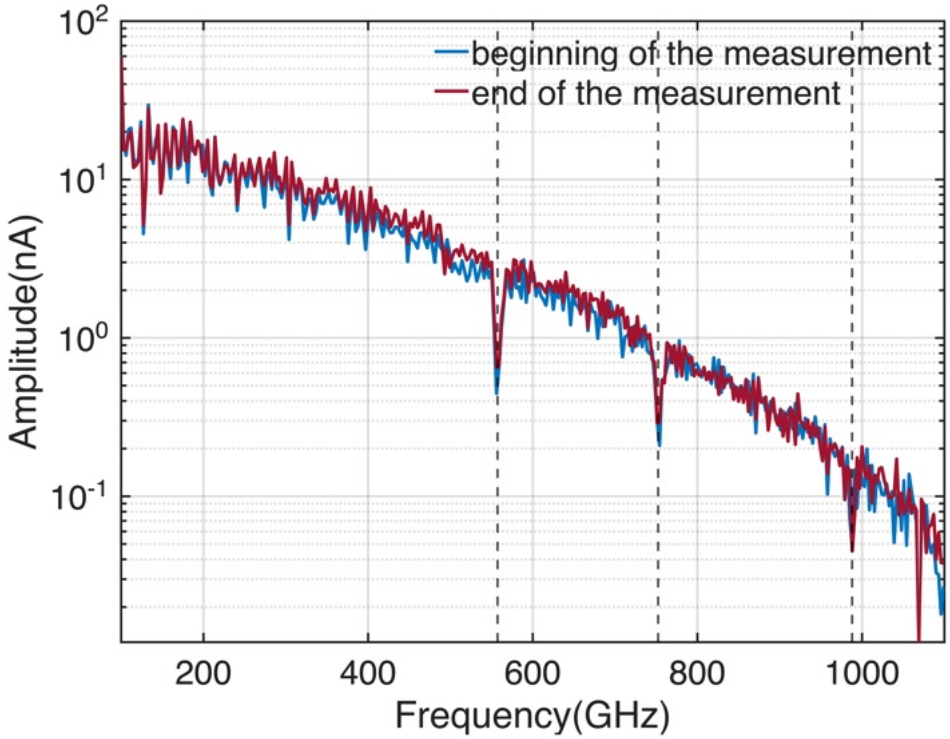

Figure 4.15 Result of the stability test, showing the amplitude of the THz signal as a function of frequency at the beginning and end of the measurement.

To further understand the origin of the inconsistencies, we investigated the modal behaviour of the waveguide. Table. 3.4 and 3.5, presents the cutoff frequencies of several modes supported by the copper waveguides and clearly demonstrates that the studied waveguides are multimode. Calculation results showing that even at the lowest frequency of $100GHz$, besides the fundamental mode, TE_{11}, higher-order modes of TE_{21} and TM_{01} are also supported. Increasing frequency increases the number of modes.

Fig. 4.16 demonstrates all the guided modes in a 3-mm-diameter copper waveguide. shows all guided TE and TM modes supported by the 3-mm-diameter copper waveguide. As the plots illustrate, the number of supported modes increases with frequency. However, in our experiment, the input signal is a center-symmetric Gaussian beam, which mainly couples to modes with angular momentum m = 1. Fig. 4.17 represents only the m = 1 modes, showing that the number of experimentally accessible modes is much smaller than the total number supported by the waveguide. Although many modes exist in theory, only a limited number is excited in practice. This distinction is important for interpreting the overall behaviour of the waveguide.

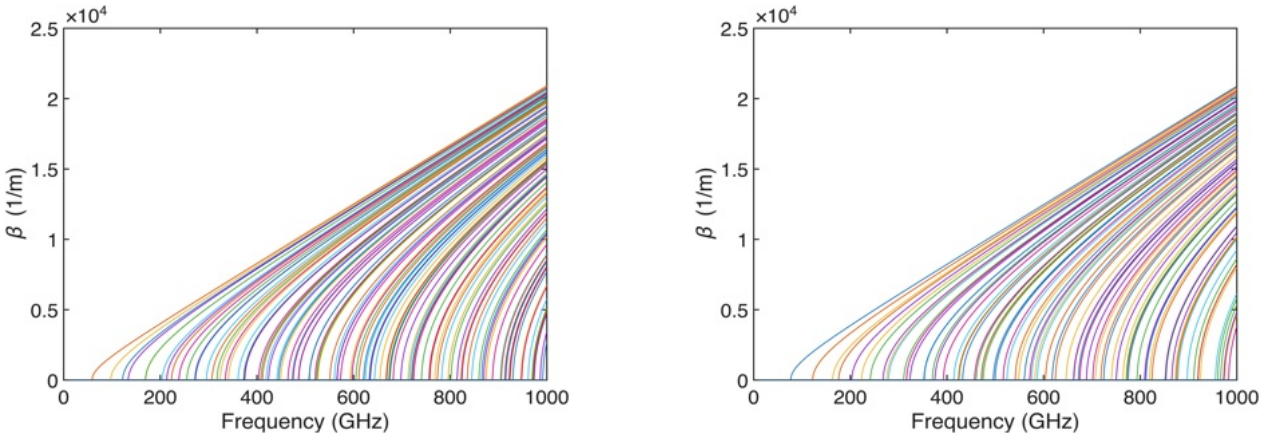

Figure 4.16 Guided modes in 3-mm-diameter copper waveguide for (a) TE, (b) TM polarization.

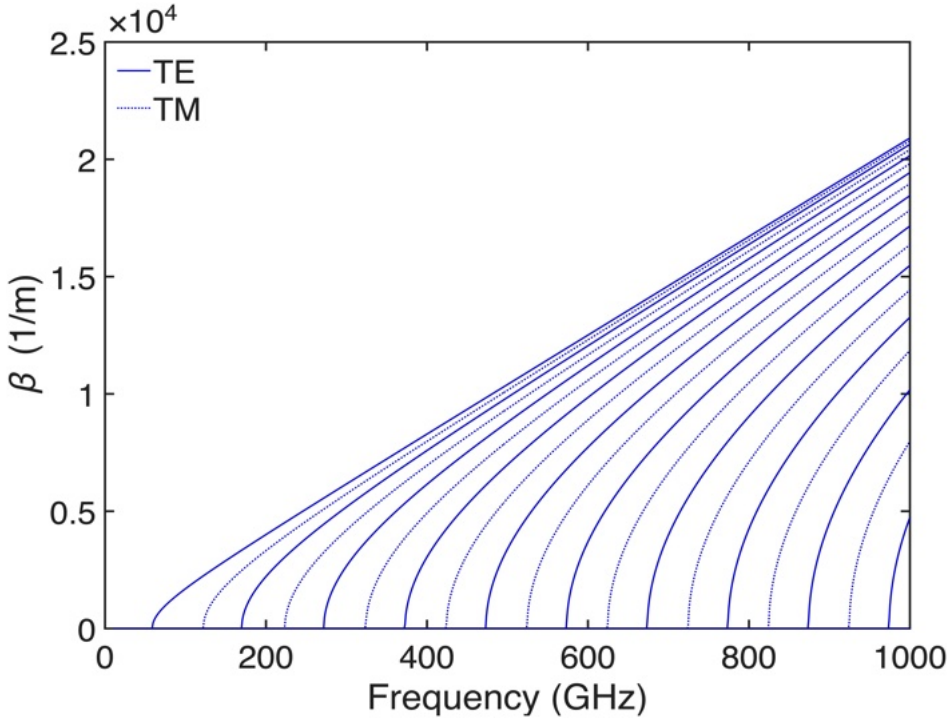

Figure 4.17 Guided modes in a 3-mm copper waveguide for m=1.

The mode profile of two guided modes in the waveguide is simulated using COMSOL and is shown in Fig. 4.18. From these results, we concluded that the experimental configuration in its current form is not sufficient for the characterization of copper waveguides. To further develop the measurement procedure, it will be necessary to optimize the coupling conditions by introducing an efficient coupling element. Such an improvement would allow selective excitation of a single mode in the waveguide.

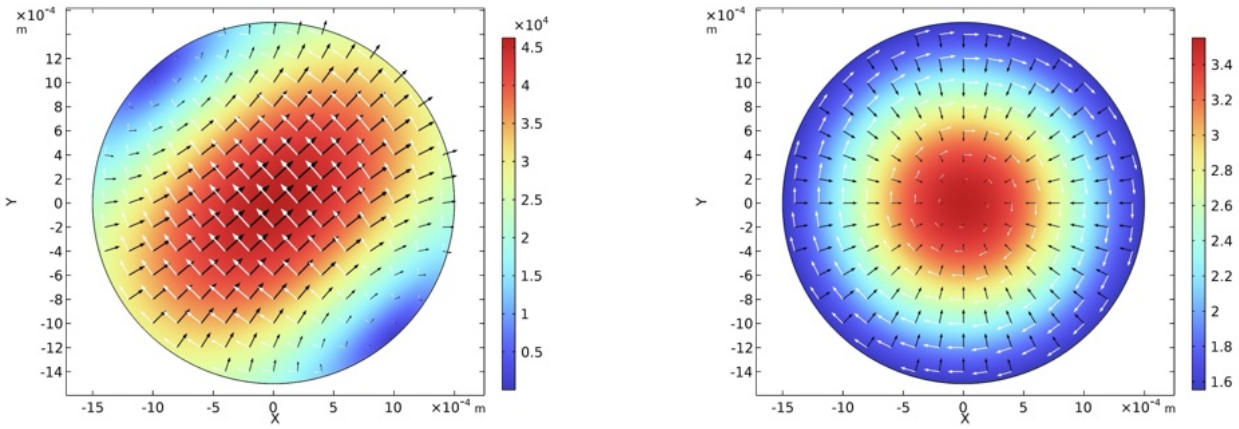

(a) (b)

Figure 4.18 Mode profile of (a) TE_{11} and (b) TE_{01}. white arrows indicate the direction of the electric field, and black arrows indicate the direction of the magnetic field inside the waveguide.

CHAPTER 5 DISCUSSION AND RECOMMENDATIONS

In this chapter, we discuss the results presented in Chapter 4 for both projects: the development of side-emitting polymer optical fibers and the terahertz characterization of copper waveguides. The key findings are analyzed in relation to the objectives and experimental observations. Finally, limitations of current approaches and potential methods for improvement are mentioned for future work.

5.1 Discussion of Side-Emission Results

5.1.1 Effect of Intrinsic Material Loss on Side Emission

The results of this work can be understood by examining several key factors that influence side emission in polymer optical fibers. First, the inherent material loss of the fiber plays an important role in the emission profile. Cutback measurements on bulk PMMA revealed an attenuation coefficient of $\alpha = 0.011 \pm 0.001\,\mathrm{cm}^{-1}$. The literature reports typical attenuation coefficients for PMMA in the visible to near-infrared range between 0.005 and 0.02 cm^{-1}, depending on purity, processing conditions, and wavelength. The measured value therefore falls within the expected range, though it is closer to the mid-to high end of the reported values. This indicates the intrinsic loss is not negligible and will contribute noticeably to the decay of transmitted power along the fiber.

The transmitted power $P(z)$ along a side-emitting fiber often is modeled as obeying a Beer–Lambert exponential decay that combines intrinsic loss (α) and side-leakage loss (often described by a side-emission coefficient). In other words, side-emitted light intensity tends to decay exponentially along the fiber, and the presence of material attenuation accelerates that decay. As the light propagates along the fiber, a fraction is absorbed. Consequently, even with an ideal scattering distribution, the transmitted power decays exponentially along the fiber, making it inherently challenging to achieve perfectly uniform emission along the fiber length. In other words, the polymer's intrinsic absorption ensures that the side emission intensity will inherently be higher near the input (where the light is strongest) and lower toward the distal end of the fiber, unless additional measures compensate for that loss.

5.1.2 Realization of Scattering Profile

Beyond intrinsic loss, a major focus of this work was the realization of controlled scattering profiles using abrasive papers to modify the fiber surface. Considering the surface modifica-

tion experiments, the results showed that introducing scattering regions on the fiber surface using an abrasive paper is an effective way to enhance side emission, but it must be controlled carefully. An unmodified fiber emits very little light through its surface (since most light stays confined in the core), whereas the surface abrasion increases the side emission, especially at the beginning of the fiber (closest to the light source), where the guided intensity is highest. At the beginning of the process, abrasion adds new scatterers on the surface, allowing more light to leak out laterally. As a result, the measured side emission is higher. However, after a certain threshold, further scratching no longer helps; instead, it either damages the surface and makes the fiber opaque or it smooths out previously created scatterers, therefore reducing the emission after the initial enhancement. Several abrasion profiles (longitudinal, transverse, and using papers with different grit sizes) were tested, and in all experiments, the result remained the same. This indicates that further enhancement of the emission is limited using the discussed method. A major controlling factor is the roughness of the abrasive paper (grit size) used for scratching. We investigated grit sizes from very rough (240) to very fine (600) to see how they differ in creating side scatterers. The results demonstrate that rougher papers produce a larger increase in emission but also reach the destructive threshold much sooner, whereas smoother papers act more gently, with smaller initial effects and a higher tolerance for multiple passes before damage occurs.

For example, using a very rough grit 240 paper, just one or two passes were enough to dramatically increase side emission. This confirms that rough abrasives can rapidly introduce many and/or large scattering sites. A slightly less rough paper (grit 320) was better. The increase in emission was more gradual. After two passes with grit 320, we saw a rise in side emission, and even after 9 passes, the emission remained elevated (in some regions even slightly higher than after 2 passes). Conversely, a finer abrasive (grit 600) produced a much more modest effect. After a couple of passes with the 600 paper, the fiber's side emission increased slightly. However, the results from Fig. 4.4d demonstrates that With smooth paper, it is difficult to create new effective scatterers; extra passes mostly smooth the surface rather than strengthening scattering.

Between different grit sizes, the grit 400 abrasive provided the best balance in our tests. A couple of scratches with grit 400 noticeably raised the side emission relative to the unmodified fiber, and in comparison, to the rougher and smoother papers, and importantly, the emission profile along the fiber was more uniform than what we saw with very rough papers. With grit 400, the intensity still tended to be higher near the input and lower at the far end, but the drop-off along the fiber was gentler. The distal sections retained more emission relative to the near sections than in the grit 240 or 320 cases. This indicates that the scatterers produced by grit 400 were more effective without immediately over-scattering or reducing

the optical power in the beginning part of the fiber.

Beyond just choosing the abrasive grit, we also experimented with how the scratching is distributed along the fiber, i.e., different scratching profiles, to further improve the uniformity of emission. One approach was to vary the number of scratches along the fiber's length in a controlled way, rather than scratching the whole fiber uniformly. As explained in 3.1.4, we divided a 1 m fiber into sections and applied fewer scratches near the input end and progressively more scratches toward the distal end. The reason was that since less light reaches the far end, we should compensate for it by increasing the emission more in the far end by producing more scatterers. Conversely, near the input, we applied only a light scratching to avoid removing too much light right at the beginning. The fiber treated with this gradient scratching profile did show improved emission in the farther sections compared to a uniformly scratched fiber. The intrinsic material loss is one reason for this remaining non-uniformity: even though we added more scatterers at the end, there was simply less light available there to scatter. There's a practical limitation, too, in how many scratches we could add at the far end before causing local damage. We found that after realizing the desired scratching profile, performing a second round of additional scratches in each section did not significantly improve the emission further. In fact, in some sections that the second round caused a slight reduction in intensity, signalling the beginning of surface degradation in those areas.

It is also worth noting that when we physically flipped the fiber end-to-end and measured the emission again, the profile remained almost identical, confirming that the measured variations were due to the distribution of scatterers we created and not an artifact of measurement orientation.

Another way we varied the modification process was by changing the orientation and sequence of scratches, including what we termed transverse scratching profiles. Up to this point, all modifications were done by polishing along the fiber length (longitudinally). We hypothesized that introducing scratches in a different orientation (for instance, transversely relative to the fiber axis) might scatter light differently and potentially increase emission or uniformity. In practice, we tried transverse scratches in successive steps. The initial introduction of transverse scratches did lead to an increase in side emission, as in the previous tests, especially near the fiber input. However, after the second profile, the input region became brighter, but the far-end sections emitted less light as we continued After applying the third transverse-scratching profile at the far end of the fiber, we observed a slight increase in emission in that region compared to the second profile. This suggested a possible trend toward a more uniform side-emission distribution when additional scratching is applied at

the weaker sections. Motivated by this indication, we proceeded to apply a fourth scratching profile to further test whether continued abrasion could improve the uniformity along the fiber length. After the fourth scratching profile, the transmission of light was limited, with most of the guided power being blocked near the fiber input and only the very beginning of the fiber receiving light. It seemed that the surface was heavily damaged or opaque. Continuing the scratching with a different grit, we observed an unexpected difference when dealing with an over-scratched fiber. By scratching the fiber with a rougher paper, we could restore the emission in lost sections, and we were able to measure the side emission in the second section of the fiber, which had previously gone dark. One possible explanation is that the many fine transverse scratches created a dense barrier that blocked the light. In contrast, the rougher paper produced larger or deeper scratches, which let more light leak out.

This observation was a key motivation for exploring sequential use of different grit sizes on the same fiber, to see if a combination of abrasives could give better results than using a single grit alone. We tried starting with a moderate grit (400), and then adding more scratches with progressively rougher papers (240 and then 120 grit). The idea was to use the smooth paper to avoid early damage and then the rougher papers to boost emission further. The result was notable. The first (grit 400) profile gave a clear increase in emission as expected, the second profile with added 240-grit scratches further raised the emission, and although the third profile (with even rougher 120-grit) caused a small dip, likely caused by slight surface degradation. This approach ultimately caused a sharp rise in emission at the sixth profile. By that point, the side emission intensity reached 90 μW, approximately double the maximum we ever got using grit 400 alone. A sequence of different grit sizes was able to overcome the saturation from a single grit and boost the emission to a higher level. This approach works because each grit size modifies the surface in a different way. A finer grit prepares the surface gently, without removing too much material, while a rougher grit that follows can introduce new scattering sites or break up areas that have become overly smooth. The difficulty is that this multi-step process requires careful control. Every additional scratch can either improve the emission or reduce it, which explains the fluctuations we observed before reaching the optimal result.

5.1.3 Limitations and Future Improvements

Considering all of these findings, several limitations and possible improvements can be identified for future work on the fabrication of side-emitting polymer optical fibers. The main limitation of the current approach is the lack of fine control and reproducibility in creating the scattering profile. Using sandpaper by hand, even with a controlled number of passes,

is inherently a low-precision method. The scattering density cannot be reproduced exactly between samples, and fine spatial control of the scatterer distribution along the fiber is not achievable. A clear improvement would be to employ a more controlled modification technique capable of producing a known and tunable scattering coefficient profile. For example, using the solutions with particles which act as the scattering particles can be considered.

Another limitation arises from the intrinsic optical loss of the polymer material. Even with an optimized scattering profile, the inherent attenuation limits how uniform the emission can occur along the fiber. In future work, the use of lower-loss polymer materials for fiber fabrication should be considered. Implementing these improvements will enhance the reproducibility, controllability, and emission uniformity of side-emitting polymer fibers, enabling their reliable use in practical applications.

5.2 Cutback Measurement of Copper Waveguides

5.2.1 Transmission Measurements and Attenuation Analysis

The loss characterization of metallic hollow waveguides in the terahertz frequency range was conducted using the cutback technique, comparing waveguides of different lengths—31 cm (straight), 117 cm (one-loop), and 204 cm (two-loop)—to extract the attenuation as a function of frequency. The general trend was a decrease in transmitted power with increasing length, as expected for a lossy metallic waveguide. Based on the cutback analysis, the attenuation of the waveguide is below 10 dB/m for the lower frequencies, increases with frequency and reaches values of approximately 15 dB/m near 1 THz, which agrees qualitatively with the expected behaviour in copper and the increasing number of supported modes at higher frequencies

Nevertheless, when repeating the measurements, the results showed a noticeable difference among the transmission spectra. Five main measurements were performed to evaluate the consistency of the result. The transmission spectra did not exactly overlap between measurements, and the extracted attenuation coefficients fluctuated beyond the expected experimental uncertainty. To determine the cause of this variation, we conducted a stability test of the THz spectroscopy system. The test demonstrated that the system is reliable. These results excluded external or instrumental sources of error and indicated that the variability originated from the coupling conditions into the waveguide.

The bending geometry of the waveguides can have another important influence on attenuation. The straight 31 cm section exhibited the highest transmission, while the 117 cm and 204 cm waveguides, which contained one and two loops respectively, showed progressively lower throughput. This is consistent with the expected bend loss in metallic waveguides,

where curved sections cause additional mode coupling and reflection at the inner and outer walls. The bend loss also increases with both the number of loops and frequency, since higher-order modes interact more strongly with the metallic boundary. The observed trend agrees qualitatively with theoretical expectations.

Surface effects of the copper waveguide also contribute to the overall loss. The inner wall roughness and potential oxidation layer increase ohmic dissipation and scattering at the boundary. Given that the THz skin depth in copper is only a few hundred nanometers, even sub-micrometre imperfections can significantly raise attenuation. The measured losses at high frequencies were higher than ideal theoretical values, indicating that such surface imperfections likely played a role.

Overall, the initial measurements provided clear attenuation trends, but their lack of reproducibility indicated that propagation inside the waveguides is strongly influenced by coupling conditions, bending, and surface quality rather than just the physical length alone.

5.2.2 Origins of Variability and Multimode Propagation Behaviour

A key factor explaining the inconsistencies in repeated measurements is the multimode nature of the copper waveguide. To further illustrate the multimode behaviour of the copper waveguide, the number of guided modes supported by a 3 mm hollow metallic tube can be estimated as a function of frequency. The cutoff frequency of the fundamental TE_{11} mode is around 39.5 GHz, while higher-order modes such as TM_{01}, TE_{21}, TE_{01} and TM_{11} sequentially appear as the frequency increases hence a large set of propagating modes is theoretically allowed.

However, because the THz beam launched into the waveguide has a Gaussian intensity profile with a central symmetry, the excitation is predominantly limited to modes with index n = 1. These modes correspond to field distributions that are symmetric around the waveguide axis and thus couple efficiently with the incident Gaussian beam. In contrast, higher-order modes with $n \neq 1$ are weakly excited.

Further evidence for multimode propagation was found in the oscillatory behaviour of the transmitted spectra. Instead of a smooth frequency-dependent transmission curve, the measured spectra showed fluctuations and local peaks. These oscillations arise from intermodal interference. Multiple modes travelling through the waveguide with slightly different phase velocities interfere constructively or destructively at the output, depending on frequency. Because the relative modal amplitudes and phases change slightly with alignment and frequency, these interference fringes also shift between repeated measurements. This behaviour

is characteristic of multimode guiding and confirms that the observed variability originates from uncontrolled mode coupling.

Another practical issue identified during the study was alignment sensitivity. Because the coupling optics had to be manually repositioned for each measurement and each waveguide length, small lateral or angular deviations between runs were unavoidable. Additionally, the free-space beam itself changed diameter and divergence across the frequency range, making it difficult to maintain consistent focusing for all frequencies. These alignment sensitivities amplify the modal coupling variability, producing non-reproducible transmission spectra.

5.2.3 Limitations and Future Improvements

The main limitation of the present setup is the lack of mode selectivity during coupling. Since the waveguide supports several modes within the measurement band, the absence of a mode filter or converter means that the launched mode distribution changed unpredictably between runs, leading to non-reproducible results. The results highlight the necessity of incorporating mode-selective coupling elements, such as tapers, to isolate the fundamental mode and achieve consistent attenuation measurements. Alternatively, using waveguides with smaller inner diameters allows single-mode operation across the desired band.

CHAPTER 6 CONCLUSION

The primary objective of this thesis was to investigate simple and effective approaches for fabricating SE-POFs and to establish reliable characterization methods for THz hollow-core waveguides. In the first part, side-emitting PMMA fibers were fabricated by modifying the fiber surface using abrasive papers of different grit sizes. The goal was to achieve a more uniform side-emission profile along the fiber length without the need for complex fabrication steps. The results demonstrated that surface modification by abrasion can substantially enhance side emission. Rougher papers (e.g., grit 240 and 320) generated strong scattering but quickly reached a destructive regime, whereas smoother papers (e.g., grit 400 and 600) produced more stable profiles. A combination of grit sizes was found to offer the best balance, enabling both improved emission and mitigation of saturation or destructive effects. Nevertheless, the emission distribution remained non-uniform, with stronger scattering near the input and gradual decay toward the distal end. These findings confirm that abrasive modification provides a simple yet limited means of controlling side emission in polymer fibers. In the second part, a cutback method was implemented to characterize the hollow-core copper waveguides in the THz frequency range. The results of the transmission measurements showed that the current measurement configuration was not optimized for the characterization of multimode waveguides.

Several limitations were encountered during this research. For the polymer fibers, the main constraint was the non-uniformity of emission along the fiber length. The use of abrasive papers, while simple and low-cost, lacks precise control and can easily degrade the guiding properties. For the copper waveguides, the principal limitation was the experimental setup. The experimental setup with the current components, while suitable for loss evaluation, was not optimized for multimode fiber characterization.

Future work on polymer side-emitting fibers should focus on developing controlled surface modification techniques capable of producing uniform and reproducible scattering profiles. For THz copper waveguides, future studies should explore experimental configurations that allow selective excitation and detection of modes. This may require implementing an optimized coupling strategy, such as a taper or adopting waveguide designs specifically engineered to support single-mode operation in the desired frequency band.

REFERENCES

[1] R. Hui and M. O'Sullivan, "Optical fiber measurement," *Fiber Optic Measurement Techniques; Elsevier: London, UK*, pp. 365–479, 2009.

[2] C.-A. Bunge *et al.*, "Special fibres and components," in *Polymer Optical Fibres*. Elsevier, 2017, pp. 119–151.

[3] L. Hasselgren, S. Galt, and S. Hard, "Diffusive optical fiber ends for photodynamic therapy: manufacture and analysis," *Applied optics*, vol. 29, no. 30, pp. 4481–4488, 1990.

[4] J. Spigulis, D. Pfafrods, and M. Stafeckis, "Optical fiber diffusive tip designs for medical laser-lightguide delivery systems," in *Biomedical Optoelectronic Devices and Systems II*, vol. 2328. SPIE, 1994, pp. 69–75.

[5] J. Spigulis *et al.*, "Side-emitting optical fibres for clinical applications," *MEDICAL AND BIOLOGICAL ENGINEERING AND COMPUTING*, vol. 34, pp. 285–286, 1996.

[6] J. Spigulis and D. Pfafrods, "Clinical potential of the side-glowing optical fibers," in *Specialty fiber optics for biomedical and industrial applications*, vol. 2977. SPIE, 1997, pp. 84–88.

[7] J. Spigulis, "Side-emitting fibers brighten our world," *Optics and photonics news*, vol. 16, no. 10, pp. 34–39, 2005.

[8] J. Kallweit *et al.*, "An overview on methods for producing side-emitting polymer optical fibers," *Textiles*, vol. 1, no. 2, pp. 337–360, 2021.

[9] C.-A. Bunge, R. Kruglov, and H. Poisel, "Rayleigh and mie scattering in polymer optical fibers," *Journal of lightwave technology*, vol. 24, no. 8, pp. 3137–3146, 2006.

[10] J. Huang *et al.*, "Evaluation of illumination intensity of plastic optical fibres with tio2 particles by laser treatment," *Autex Research Journal*, vol. 15, no. 1, pp. 13–18, 2015.

[11] C.-A. Bunge *et al.*, "Directed illumination by side-emitting fibers with trilobal cross section," *Journal of Lightwave Technology*, vol. 37, no. 22, pp. 5714–5721, 2019.

[12] J. Spigulis *et al.*, "Glowing optical fiber designs and parameters," in *Optical inorganic dielectric materials and devices*, vol. 2967. SPIE, 1997, pp. 231–236.

[13] C. Zheng *et al.*, "Femtosecond laser fabrication of cavity microball lens (cmbl) inside a pmma substrate for super-wide angle imaging," *small*, vol. 11, no. 25, pp. 3007–3016, 2015.

[14] A. Reupert *et al.*, "Side-emission properties of femtosecond laser induced scattering centers in optical fibers," *Optical Materials Express*, vol. 9, no. 6, pp. 2497–2510, 2019.

[15] G.-L. Roth, C. Esen, and R. Hellmann, "Femtosecond laser direct generation of 3d-microfluidic channels inside bulk pmma," *Optics Express*, vol. 25, no. 15, pp. 18 442–18 450, 2017.

[16] M. H. Im *et al.*, "Modification of plastic optical fiber for side-illumination," in *International Conference on Human-Computer Interaction*. Springer, 2007, pp. 1123–1129.

[17] V. Koncar, "Optical fiber fabric displays," *Optics and Photonics news*, vol. 16, no. 4, pp. 40–44, 2005.

[18] J. Shen *et al.*, "Light-emitting fabrics integrated with structured polymer optical fibers treated with an infrared co2 laser," *Textile Research Journal*, vol. 83, no. 7, pp. 730–739, 2013.

[19] J. Shen, C. Chui, and X. Tao, "Luminous fabric devices for wearable low-level light therapy," *Biomedical Optics Express*, vol. 4, no. 12, pp. 2925–2937, 2013.

[20] R. Seewald *et al.*, "Use of uv-curing adhesive systems on non-transparent joining parts by using sidelight activated polymer optical fibres," in *Industrial Applications of Adhesives: 1st International Conference on Industrial Applications of Adhesives*. Springer, 2020, pp. 1–14.

[21] R. George and L. J. Walsh, "Performance assessment of novel side firing flexible optical fibers for dental applications," *Lasers in Surgery and Medicine: The Official Journal of the American Society for Laser Medicine and Surgery*, vol. 41, no. 3, pp. 214–221, 2009.

[22] U. Ali, K. J. B. A. Karim, and N. A. Buang, "A review of the properties and applications of poly (methyl methacrylate)(pmma)," *Polymer Reviews*, vol. 55, no. 4, pp. 678–705, 2015.

[23] R. Inglev *et al.*, "Polymer optical fiber modification by etching using hansen solubility parameters—a case study of TOPAS, Zeonex, and PMMA," *Journal of Lightwave Technology*, vol. 37, no. 18, pp. 4776–4783, 2019.

[24] X. Hu, K. Yang, and C. Zhang, "Optimization of preparation conditions for side-emitting polymer optical fibers using response surface methodology," *Polymers*, vol. 12, no. 12, p. 3062, 2020.

[25] P. Dyer, "Excimer laser polymer ablation: twenty years on," *Applied Physics A*, vol. 77, no. 2, pp. 167–173, 2003.

[26] S. Prakash and S. Kumar, "Experimental investigations and analytical modeling of multi-pass co2 laser processing on pmma," *Precision Engineering*, vol. 49, pp. 220–234, 2017.

[27] D. Zaremba and R. Evert, "Materials, chemical properties and analysis," in *Polymer optical fibres*. Elsevier, 2017, pp. 153–186.

[28] M. Radovanovic and M. Madic, "Experimental investigations of co2 laser cut quality: a review," *Nonconventional Technologies Review*, vol. 4, no. 4, p. 35, 2011.

[29] B. M. Quandt *et al.*, "Pof-yarn weaves: controlling the light out-coupling of wearable phototherapy devices," *Biomedical optics express*, vol. 8, no. 10, pp. 4316–4330, 2017.

[30] J. Wang, B. Huang, and B. Yang, "Effect of weave structure on the side-emitting properties of polymer optical fiber jacquard fabrics," *Textile Research Journal*, vol. 83, no. 11, pp. 1170–1180, 2013.

[31] F. Jiménez *et al.*, "Numerical simulation of light propagation in plastic optical fibres of arbitrary 3d geometry," *WSEAS Trans. Math*, vol. 3, pp. 824–829, 2004.

[32] B. Lustermann *et al.*, "Experimental determination and ray-tracing simulation of bending losses in melt-spun polymer optical fibres," *Scientific reports*, vol. 10, no. 1, p. 11885, 2020.

[33] N. Jing *et al.*, "Investigation of a macrobending micro-plastic optical fiber for refractive index sensing," *Applied optics*, vol. 53, no. 34, pp. 8145–8150, 2014.

[34] W.-C. Wang *et al.*, "A shear and plantar pressure sensor based on fiber-optic bend loss." *Journal of Rehabilitation Research & Development*, vol. 42, no. 3, 2005.

[35] Z. Guo *et al.*, "Study of macro-bending biconical tapered plastic optical fiber for relative humidity sensing," *Sensor Review*, vol. 39, no. 3, pp. 352–357, 2019.

[36] J. Wang *et al.*, "Design and development of polymeric optical fiber jacquard fabric with dynamic pattern display," *Textile Research Journal*, vol. 82, no. 10, pp. 967–974, 2012.

[37] L. Ge and J. Tan, "Development of three-dimensional effects and stretch for polymeric optical fiber (pof) textiles with double weave structure containing spandex," *The Journal of The Textile Institute*, vol. 112, no. 3, pp. 398–405, 2021.

[38] D. Křemenáková *et al.*, "Characterization of side emitting plastic optical fibers light intensity loss," *World Journal of Engineering*, vol. 10, no. 3, pp. 223–228, 2013.

[39] E. De la Rosa-Cruz *et al.*, "Characterization of fluorescence induced by side illumination of rhodamine b doped plastic optical fibers," *Fiber & Integrated Optics*, vol. 20, no. 5, pp. 457–464, 2001.

[40] P. Kröplin *et al.*, "Overview of the pof market," in *Polymer Optical Fibres*. Elsevier, 2017, pp. 349–400.

[41] L. Slooff *et al.*, "Rare-earth doped polymers for planar optical amplifiers," *Journal of applied physics*, vol. 91, no. 7, pp. 3955–3980, 2002.

[42] Y. Li *et al.*, "Review on the role of polymers in luminescent solar concentrators," *Journal of Polymer Science Part A: Polymer Chemistry*, vol. 57, no. 3, pp. 201–215, 2019.

[43] R. Inman *et al.*, "Cylindrical luminescent solar concentrators with near-infrared quantum dots," *Optics express*, vol. 19, no. 24, pp. 24 308–24 313, 2011.

[44] J. Guo *et al.*, "Stretchable and temperature-sensitive polymer optical fibers for wearable health monitoring," *Advanced Functional Materials*, vol. 29, no. 33, p. 1902898, 2019.

[45] K. Jakubowski *et al.*, "Luminescent solar concentrators based on melt-spun polymer optical fibers," *Materials & Design*, vol. 189, p. 108518, 2020.

[46] J. LUO and Q. GAO, "Z. kaiyan, ge mingqiao, liu jialin, structure and luminescent properties of luminous polypropylene fiber based on sr2mgsi2o7: Eu2+, dy3+," *J. Rare Earths*, vol. 32, no. 8, pp. 696–701, 2014.

[47] W. Ding *et al.*, "Stretchable multi-luminescent fibers with aiegens," *Journal of Materials Chemistry C*, vol. 7, no. 35, pp. 10 769–10 776, 2019.

[48] A. Erdman *et al.*, "Luminescent cellulose fibers modified with poly ((9-carbazolyl) methylthiirane)," *Polymers*, vol. 12, no. 10, p. 2296, 2020.

[49] F. Jakobs *et al.*, "Homogeneous distribution of polymerizable coumarin dyes for active few mode pof," *Materials*, vol. 13, no. 8, p. 1975, 2020.

[50] I. Parola *et al.*, "Fabrication and characterization of polymer optical fibers doped with perylene-derivatives for fluorescent lighting applications," *Fibers*, vol. 5, no. 3, p. 28, 2017.

[51] M. Beckers *et al.*, "An overview on fabrication methods for polymer optical fibers," *Polymer International*, vol. 64, no. 1, pp. 25–36, 2015.

[52] K. Jakubowski *et al.*, "Recent advances in photoluminescent polymer optical fibers," *Current Opinion in Solid State and Materials Science*, vol. 25, no. 3, p. 100912, 2021.

[53] M. Tonouchi, "Cutting-edge terahertz technology," *Nature photonics*, vol. 1, no. 2, pp. 97–105, 2007.

[54] D. M. Mittleman, "Perspective: Terahertz science and technology," *Journal of Applied Physics*, vol. 122, no. 23, 2017.

[55] A. Leitenstorfer *et al.*, "The 2023 terahertz science and technology roadmap," *Journal of Physics D: Applied Physics*, vol. 56, no. 22, p. 223001, 2023.

[56] R. M. Woodward *et al.*, "Terahertz pulse imaging in reflection geometry of human skin cancer and skin tissue," *Physics in Medicine & Biology*, vol. 47, no. 21, p. 3853, 2002.

[57] G. Xu and M. Skorobogatiy, "Wired thz communications," *Journal of infrared, millimeter, and terahertz waves*, vol. 43, no. 9, pp. 728–778, 2022.

[58] G. P. Agrawal, *Fiber-optic communication systems*. John Wiley & Sons, 2012.

[59] F. Poli, A. Cucinotta, and S. Selleri, *Photonic crystal fibers: properties and applications*. Springer, 2007.

[60] J. C. Knight *et al.*, "Photonic band gap guidance in optical fibers," *Science*, vol. 282, no. 5393, pp. 1476–1478, 1998.

[61] L. Vincetti and V. Setti, "Waveguiding mechanism in tube lattice fibers," *Optics express*, vol. 18, no. 22, pp. 23 133–23 146, 2010.

[62] R. Beravat *et al.*, "Twist-induced guidance in coreless photonic crystal fiber: A helical channel for light," *Science Advances*, vol. 2, no. 11, p. e1601421, 2016.

[63] H. Li *et al.*, "Terahertz fiber devices," *APL Photonics*, vol. 10, no. 2, 2025.

[64] M. S. Islam *et al.*, "Terahertz optical fibers," *Optics express*, vol. 28, no. 11, pp. 16 089–16 117, 2020.

[65] R. McGowan, G. Gallot, and D. Grischkowsky, "Propagation of ultrawideband short pulses of terahertz radiation through submillimeter-diameter circular waveguides," *Optics Letters*, vol. 24, no. 20, pp. 1431–1433, 1999.

[66] T. Hidaka *et al.*, "Ferroelectric pvdf cladding terahertz waveguide," *Journal of lightwave technology*, vol. 23, no. 8, p. 2469, 2005.

[67] J. A. Harrington *et al.*, "Hollow polycarbonate waveguides with inner cu coatings for delivery of terahertz radiation," *Optics Express*, vol. 12, no. 21, pp. 5263–5268, 2004.

[68] B. Bowden, J. A. Harrington, and O. Mitrofanov, "Silver/polystyrene-coated hollow glass waveguides for the transmission of terahertz radiation," *Optics letters*, vol. 32, no. 20, pp. 2945–2947, 2007.

[69] ——, "Fabrication of terahertz hollow-glass metallic waveguides with inner dielectric coatings," *Journal of Applied Physics*, vol. 104, no. 9, 2008.

[70] K. Bhowmik and G.-D. Peng, "Polymer optical fibers," in *Handbook of optical fibers*. Springer, 2019, pp. 967–1017.

[71] D. M. Pozar, "Microwave engineering," *Fourth Edition; Wiley: Hoboken, NJ, USA*, pp. 120–130, 2012.

[72] D. Diso, M. Perrone, and M. Protopapa, "Beam width measurements of asymmetric multi-mode laser beams," *Optics & Laser Technology*, vol. 31, no. 6, pp. 411–418, 1999.

APPENDIX A DESIGN OF THE INTEGRATING ELEMENT

To relate the model of (2.1) to measurements, we require a method that collects a fixed and reproducible fraction of the side-emitted power. We therefore design an integrating element intended to capture essentially all radiation leaving the fiber within the detector's acceptance and to redirect it to a single detector.

The element consists of an ellipsoidal cavity with a cut-out of height h for the detector (set by the mechanical enclosure). The fiber end face and the detector are placed at the two foci of the ellipse. We define D as the fiber-detector separation fixed by the setup, and H as the fiber-reflector distance to be optimized. The polar angle $\theta \in [0, \theta_{\max}]$ is measured from the fiber axis within the reflector, and θ_{capture} denotes the largest emission angle that is redirected onto the detector. The detector has a finite angular size θ_{det} as viewed from the fiber. For a given geometry, the maximum collection is achieved when $\theta_{\text{capture}} = \pi - \theta_{\text{det}}$. The reflector profile $r(\theta)$ is obtained from the constant optical path length from the fiber to the reflector and then to the detector. Using standard ellipse relations, the required parametric curve satisfies

$$r(\theta) + \sqrt{\Big(D - r(\theta)\cos\theta\Big)^2 + \Big(r(\theta)\sin\theta\Big)^2} = D + 2H. \tag{A.1}$$

The detector angular size follows from the slot height,

$$\tan\theta_{\text{det}} = \frac{h}{2D}. \tag{A.2}$$

At optimal capture, the boundary ray at $\theta_{\max}$ must graze the detector aperture, which gives

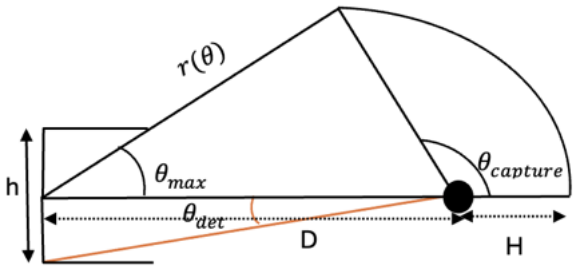

Figure A.1 Schematic of a light integrating element.

the geometric condition

$$\tan(\pi - \theta_{\text{capture}}) = \tan\theta_{\text{det}} = \frac{r(\theta_{\max})\sin\theta_{\max}}{D - r(\theta_{\max})\cos\theta_{\max}}. \tag{A.3}$$

Let $r_0 = r(\theta_{\max})$. Solving eq.A.3 for r_0 yields

$$r_0 = \frac{D\ \tan\theta_{\text{det}}}{\sin\theta_{\max} + \cos\theta_{\max}\tan\theta_{\text{det}}}. \tag{A.4}$$

Eliminating $r(\theta)$, one obtains an explicit relation between r_0, D, $\theta_{\max}$, and the design parameter H. Rearranging first gives

$$r_0 = 2H\,\frac{D+H}{D(1-\cos\theta_{\max}) + 2H}, \tag{A.5}$$

from which the optimal H is

$$H = \frac{r_0 - D}{2} + \sqrt{\left(\frac{r_0 - D}{2}\right)^2 + r_0 D\,\sin^2\left(\frac{\theta_{\max}}{2}\right)}. \tag{A.6}$$

Equations. A.4- A.6 provide a constructive procedure to choose H for a specified detector size h, working distance D, and capture angle $\theta_{\max}$.

Experimental efficiency of the light-integrating element. We characterize the element by an experimental efficiency η, defined as the fraction of the locally side-emitted power that is delivered to the detector. Over a short segment ΔL in which the scattering coefficient is approximately constant and equal to δ_0, the measured ratio between the side signal I_s

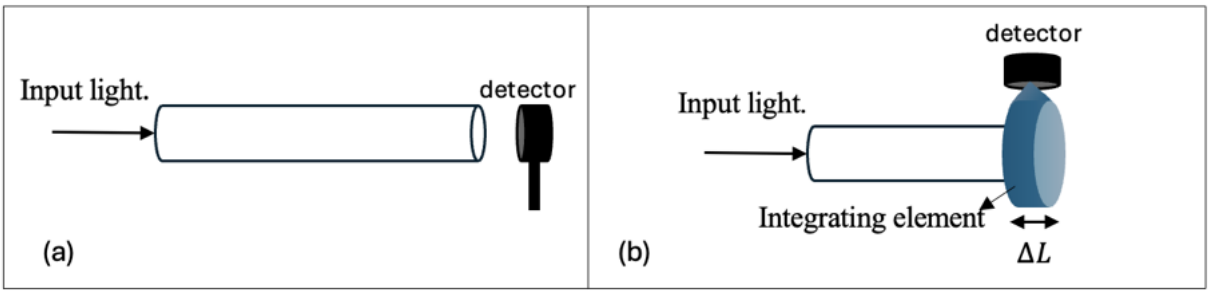

Figure A.2 Schematic of the setup with integrating element to measure (a) I_{out} and (b) I_s

(collected by the integrating element) and the endface signal I_{out} obeys

$$\frac{I_s}{I_{\text{out}}} = \delta_0 \, \Delta L \, \eta. \tag{A.7}$$

Here I_{out} is the power emerging from the fiber end, while I_s is the power redirected by an integrating element of length ΔL and measured at the same detector. A one-time calibration with a region of known δ_0 thus determines η. Thereafter, scanning the element along the fiber allows a direct estimate of the local side-scattering coefficient $\delta(z)$.

APPENDIX B FIBER DRAWING PARAMETERS FOR FABRICATION OF PMMA FIBER

Table B.1 Preform preparation and drawing conditions for PMMA fiber fabrication

Step	Details
Preform	PMMA rod, 1” diameter, purchased from McMaster Carr
Preform preparation	Degassed for 2 weeks at 90°C
Preheating time	2 h
Preheating temperatures	$T_{\text{top}} = 115$°C, $T_{\text{down}} = 115$°C
Drawing time	4 h
Drawing temperatures	$T_{\text{top}} = 115$°C, $T_{\text{down}} = 190$°C
Drawing speed range	100–440 mm/min
Resulting fiber diameter range	0.8–1.7 mm